Decapping activators Edc3 and Scd6 act redundantly with Dhh1 in post-transcriptional repression of starvation-induced pathways

Rakesh Kumar[1#], Fan Zhang[1#], Shreyas Niphadkar[3], Chisom Onu[2], Anil Kumar Vijjamarri[1], Miriam L. Greenberg[2], Sunil Laxman[3], and Alan G. Hinnebusch[1]

[1]Division of Molecular and Cellular Biology, Eunice Kennedy Shriver National Institute of Child Health and Human Development, National Institutes of Health, Bethesda, MD

[2]Department of Biological Sciences, Wayne State University, Detroit, MI

[3]Institute for Stem Cell Science and Regenerative Medicine (DBT-inStem) GKVK Post Bellary Road Bangalore 560065

#Contributed equally

ABSTRACT

Degradation of many yeast mRNAs involves decapping by the Dcp1:Dcp2 complex. Previous studies on decapping activators Edc3 and Scd6 suggested their limited roles in mRNA decay. RNA-seq analysis of mutants lacking one or both proteins revealed that Scd6 and Edc3 have largely redundant activities in targeting numerous mRNAs for degradation that are masked in the single mutants. These transcripts also are frequently targeted by decapping activators Dhh1 and Pat1, and the collective evidence suggests that Scd6/Edc3 act interchangeably to recruit Dhh1 to Dcp2. Ribosome profiling shows that redundancy between Scd6 and Edc3 and their functional interactions with Dhh1 and Pat1 extend to translational repression of particular transcripts, including a cohort of poorly translated mRNAs displaying interdependent regulation by all four factors. Scd6/Edc3 also participate with Dhh1/Pat1 in post-transcriptional repression of proteins required for respiration and catabolism of alternative carbon sources, which are normally expressed only in limiting glucose. Simultaneously eliminating Scd6/Edc3 increases mitochondrial membrane potential and elevates metabolites of the tricarboxylic acid and glyoxylate cycles typically observed only during growth in low glucose. Thus, Scd6/Edc3 act redundantly, in parallel with Dhh1 and in cooperation with Pat1, to adjust gene expression to nutrient availability by controlling mRNA decapping and decay.

INTRODUCTION

Degradation of mRNA is a key aspect of gene expression that can be regulated in response to nutrient availability, cell stress, and developmental pathways in eukaryotic cells and also serves to eliminate defective mRNAs. A major pathway of cytoplasmic mRNA turnover involves truncating the poly(A) tail by the Ccr4/Not and Pan2/Pan3 complexes, followed by removal of the m^7G cap by the Dcp1/Dcp2 decapping complex and 5' to 3' exonucleolytic degradation by Xrn1. The decapping complex is activated by factors that interact with low-complexity sequence motifs in the C-terminal tail (CTT) of the catalytic subunit Dcp2, including Edc3, Scd6, DEAD-box helicase Dhh1, and Pat1, which also interact with one another extensively. There is evidence that Pat1 is recruited to oligoadenylate tails remaining on mRNAs following partial deadenylation, in association with the Lsm1-Lsm7 complex, and activates decapping via interactions with other decapping activators and with the Dcp2 CTT itself (Parker 2012) (He and Jacobson 2023)

Genome-wide analysis of mRNA abundance (RNA-seq) in yeast mutants lacking Dhh1 or Pat1 suggested that only ~40-50% of mRNAs up- or down-regulated in one mutant were also similarly dysregulated in the other mutant, suggesting that many mRNAs are targeted for degradation exclusively by Pat1 or Dhh1 (He et al. 2018). By also determining mRNA changes in a *pat1Δdhh1Δ* double mutant, we uncovered more extensive functional cooperation by Pat1 and Dhh1 in targeting ~75% of mRNAs up-regulated in the single mutants, as a fraction of mRNAs were derepressed only in the double mutant (Vijjamarri et al. 2023a). The majority of mRNAs derepressed by *dhh1Δ* or *pat1Δ* mutations are likewise up-regulated in *dcp2Δ* cells (He et al. 2018), their derepression on eliminating Dhh1 is largely dependent on Dcp2, and they

exhibit greater than average proportions of decapped mRNAs in WT cells but not in the *dhh1Δ* or *pat1Δ* mutant (Vijjamarri et al. 2023a)—all consistent with Dhh1/Pat1 targeting mRNAs for degradation via decapping. Moreover, more than half of the mRNAs up-regulated by *dcp2Δ* are likewise up-regulated by *dhh1Δ* and/or *pat1Δ,* whereas most of the remaining 45% of Dcp2-repressed transcripts are targeted primarily by the Upf factors responsible for nonsense-mediated mRNA decay (NMD) (Vijjamarri et al. 2023b), which represses a large cohort of natural NMD targets in WT cells (Celik et al. 2017).

The cumulative contributions of Dhh1 and Pat1 to mRNA decay via decapping is consistent with their independent interactions with distinct segments of the Dcp2 CTT (He et al. 2018), which appears to be direct for Pat1 but bridged by Edc3 or Scd6 for Dhh1. There is also evidence for distinct decapping complexes containing either Dhh1 or Pat1 in addition to Xrn1, Edc3 or Scd6 (He et al. 2022). However, Dhh1 occupancy determined by RIP-Seq analysis (Miller et al. 2018), tends to be elevated for mRNAs derepressed by either *dhh1Δ* (23) or *pat1Δ* (Vijjamarri et al. 2023a), consistent with Dhh1 contributing to degradation of many mRNAs targeted by Pat1. In accordance with overlapping roles for Pat1 and Dhh1, Pat1 binding to the Dcp2 CTT was required for degradation of certain Dhh1-targeted mRNAs only when Dhh1 recruitment to the CTT was compromised (He et al. 2022).

There is evidence that Edc3 is a common constituent of decapping complexes containing Xrn1 and one or more of the decapping activators Dhh1, Pat1, Scd6, and Upf1 (He et al. 2022). It is surprising therefore that Edc3 has been implicated in targeting only two transcripts for degradation, *YRA1* and *RPS28B* (Badis et al. 2004; Dong et al. 2007). Edc3 shares sequence similarity with decapping activator Scd6 and both proteins contain an FDF motif shown to

interact competitively with the Dhh1 homolog in animal systems (Tritschler et al. 2008; Tritschler et al. 2009). Yeast Edc3 contains two other segments besides the FDF motif that likely comprise a tripartite interaction surface for Dhh1 (Sharif et al. 2013). Edc3 and Scd6 also share N-terminal LSm domains that compete for binding to helical-leucine-rich (HLM) motifs in the yeast Dcp2 CTT (Fromm et al. 2012), an interaction that appears to activate decapping by overcoming an autoinhibitory element in Dcp2 (He and Jacobson 2015) (Paquette et al. 2018). Analyzing effects of deleting the Edc3 interaction site in the Dcp2-CTT on levels of several Dhh1-repressed mRNAs suggested that recruitment of Dhh1 to Dcp2 can be mediated interchangeably by Edc3 or Scd6 bound to the same site in the Dcp2 CTT (He et al. 2022). These findings, plus the fact that deleting *SCD6* and *EDC3* simultaneously confers a synthetic growth defect (Decourty et al. 2008), suggest that Scd6 and Edc3 might function redundantly in targeting specific mRNAs for decapping and degradation.

Although tethering Dhh1 or Scd6 enhances degradation of reporter mRNAs via Dcp1/Dcp2 (Carroll et al. 2011; Sweet et al. 2012; Zeidan et al. 2018), it is not well understood how these factors are targeted to specific native mRNAs. Dhh1 has been implicated in accelerating degradation associated with non-optimal codons in yeast mRNAs (Presnyak et al. 2015), being required for the rapid turnover conferred by suboptimal codons inserted in reporter mRNAs (Sweet et al. 2012). A queue of slowly elongating ribosomes upstream from non-optimal codons can be recognized by Dhh1, and overexpressing or tethering Dhh1 evokes ribosome stalling at non-optimal codons. Dhh1 association and Dhh1-dependent repression of mRNA abundance both correlate with codon non-optimality across the yeast transcriptome (Radhakrishnan et al. 2016). Structural evidence suggests that ribosomes stalled at suboptimal codons with an empty

A site are recognized by Not5 binding to the ribosomal E-site to elicit Dhh1 recruitment and increased mRNA decapping and degradation (Buschauer et al. 2020). Dcp2, Pat1, and the deadenylase subunits of the Ccr4/Not complex also contribute to this process (Radhakrishnan et al. 2016; Webster et al. 2018). Despite these findings, the sets of mRNAs found to be most highly up-regulated in *dhh1Δ* and *pat1Δ* cells are not enriched for suboptimal codons and are generally well-translated in WT cells, suggesting that other features of these transcripts are responsible for their preferential targeting by Dhh1 or Pat1 for decapping/decay (Vijjamarri et al. 2023a).

In addition to regulating mRNA degradation, there is evidence that Pat1, Dhh1, and Scd6 can repress mRNA translation. Tethering Dhh1 or Scd6 represses translation of reporter mRNAs in *dcp2Δ* mutant cells where the tethered transcripts cannot be decapped and degraded (Carroll et al. 2011; Sweet et al. 2012; Zeidan et al. 2018), functioning either during elongation (Dhh1) or the initiation stage (Scd6) of translation. Deletion of Dhh1 and Pat1 simultaneously eliminated loss of bulk polysomes evoked by nutrient starvation and also increased initiation rates of certain mRNAs (Holmes et al. 2004) (Coller and Parker 2005) (Arribere et al. 2011). Supporting a direct role in repressing translation, overexpressing Dhh1 or Pat1 in nonstarved cells evoked polysome disassembly and reduced the initiation rate of specific mRNAs; and addition of Dhh1 (Coller and Parker 2005) or N-terminally truncated Pat1 (Nissan et al. 2010) to yeast extracts inhibited bulk translation and 48S preinitiation complex (PIC) assembly in vitro. Ribosome profiling studies of *dhh1Δ, pat1Δ* and *pat1Δdhh1Δ* mutants identified hundreds of mRNAs for particular genes that appear to be translationally repressed or activated by Dhh1 or Pat1 in nutrient-replete cells (Jungfleisch et al. 2017) (Radhakrishnan et al. 2016; Zeidan et al. 2018), which frequently involves cooperation between Dhh1 and Pat1 (Vijjamarri et al. 2023a).

Interestingly, a fraction of mRNAs showed translational repression by Dhh1 that required Dcp2 and exhibit high proportions of decapped degradation intermediates in WT cells, suggesting translational repression via Dhh1-stimulated decapping that precedes mRNA turnover (Vijjamarri et al. 2023b).

Recently, we showed that Pat1 and Dhh1 function with the decapping enzyme in rich medium to repress the abundance or translation of numerous mRNAs encoding proteins required specifically in media containing an alternative carbon or nitrogen source (Vijjamarri et al. 2023a; Vijjamarri et al. 2023b). These include many of the mitochondrial proteins involved in oxidative phosphorylation (Ox. Phos.), and Pat1, Dhh1 and Dcp2 are required for the low mitochondrial membrane potential in glucose-replete cells expected from low electron transport chain (ETC) activity. Mutants lacking Dcp2, Dhh1, or Pat1 also display impaired mRNA turnover or elevated translation of mRNAs subject to carbon or nitrogen catabolite transcriptional repression in WT cells in rich medium. Related to this, Pat1 cooperates with Dhh1 (Hu et al. 2015) in repressing mRNAs encoding factors for autophagy and helps to suppress this pathway in rich medium. Pat1 further assists Dcp2 in post-transcriptional repression of mRNAs encoding cell adhesion proteins, critical for forming adhesion-linked chains of elongated cells able to penetrate substrates, thereby repressing invasive cell growth on nutrient-rich agar medium (Vijjamarri et al. 2023a; Vijjamarri et al. 2023b).

In this study, we employed RNA-Seq and ribosome profiling to determine whether Edc3 and Scd6 have largely redundant functions in targeting mRNAs for decapping and attendant degradation, and whether they functionally cooperate with Pat1 or Dhh1 in repressing the abundance or translation of particular mRNAs. We also sought to determine whether Edc3/Scd6

participate with Pat1/Dhh1 and the decapping enzyme in conferring post-transcriptional repression in rich medium of genes normally well-expressed only in nutrient-deprived cells. We find that a mutant lacking both Edc3 and Scd6 exhibits increased abundance of a cohort of mRNAs that are up-regulated only when both factors are eliminated, and which occurs without increased transcription of the cognate genes, signifying reduced decapping and degradation in mutant cells lacking both factors. These transcripts are also generally derepressed in *dcp2Δ* cells, and in cells lacking Pat1 or Dhh1, and show enrichment for Dhh1 occupancy. A strikingly similar pattern of mRNA derepression observed in the *dhh1Δ* and *scd6Δedc3Δ* mutants supports the notion that Edc3/Scd6 act redundantly to recruit Dhh1 to Dcp2 for activation of decapping (He et al. 2022). We also observed functional redundancy between Scd6 and Edc3 and cooperation with Dhh1/Pat1 in repressing translation of particular mRNAs, with evidence for interdependent repression by all four decapping factors. Importantly, Edc3/Scd6 also contribute to the post-transcriptional repression of proteins required for catabolism of non-preferred carbon or nitrogen sources on rich medium, including Ox. Phos. proteins, acting collectively to enhance glucose repression, maintain low-level mitochondrial electron transport and reduce levels of tricarboxylic acid (TCA) and glyoxylate cycle intermediates in glucose-replete cells. Together, our findings indicate that Edc3 and Scd6 have redundant functions in stimulating degradation or translational repression of transcripts targeted in parallel by Dhh1 and Pat1 to promote post-transcriptional repression in rich medium of factors normally up-regulated only in nutrient-deprived cells.

METHODS

Yeast strains and plasmids.

The following yeast strains were employed for all experiments: WT strain HFY114 (W303: *MATa ade2-1 ura3-1 his3-11,15 trp1-1 leu2-3,112 can1-100*) (He et al. 2003), *scd6Δ* strain SYY2352 (*MATa ade2-1 ura3-1 his3-11,15 trp1-1 leu2-3,112 can1-100 scd6Δ::kanMX6*) (He and Jacobson 2015), *edc3Δ* strain FZY862 (*MATa ade2-1 ura3-1 his3-11,15 trp1-1 leu2-3,112 can1-100 edc3Δ::kanMX4*), and *scd6Δedc3Δ* strain FZY858 (*MATa ade2-1 ura3-1 his3-11,15 trp1-1 leu2-3,112 can1-100 scd6Δ::hphMX4 edc3Δ::kanMX4*).

Strains FZY858 and FZY862 were generated by replacing chromosomal *EDC3* in strains FZY855 and HFY114, respectively, with the *edc3Δ::kanMX4* allele amplified by PCR from the chromosomal DNA of strain 255 (*MATa his3Δ1 leu2Δ0 met15Δ0 ura3Δ0 edc3Δ::kanMX4*) obtained from Research Genetics. DNA sequences up to 310 bp upstream and 340 bp downstream of the *EDC3* coding sequence were included in the amplified fragment used for transformation of FZY855 and HFY114 to G418-resistance. FZY855 was derived from SYY2352 by transforming with marker-swap plasmid pAG32 (Goldstein and McCusker 1999) to replace *scd6Δ::kanMX6* with *scd6Δ::hphMX6,* selecting for resistance to hygromycin and screening for loss of G418-resistance. The presence of all deletion alleles was verified by PCR analysis of chromosomal DNA. A complete list of yeast strains employed is given in Table S1.

Plasmids pLfz614-7 and pLfz635-5 contain the *EDC3* CDS with 420 bp upstream and 490 bp downstream, on a ~2.6 kb fragment, and plasmids pL615-5 and pLfz636-1 contain the *SCD6* CDS with 500 bp upstream and 180 bp downstream on a ~1.7 kb fragment, amplified by PCR from yeast genomic DNA and inserted between the XhoI and EcoRI sites of YCplac33 or YCplac111, respectively. The inserted yeast DNA fragments were verified by sequencing in their entirety. A complete list of plasmids employed is given in Table S2.

Cell spotting growth assays

Yeast transformants harboring plasmids containing *EDC3*, *SCD6,* or empty vector were grown to mid-logarithmic phase at 30°C in liquid synthetic complete medium (SC) without uracil (SC-U). Cultures were diluted to OD_{600} of 1.0 and 10-fold serial dilutions were spotted on agar medium of the same composition and incubated at 30°C or 37°C for 2 days.

Polysome profiling

Polysome profiling was conducted as described previously (Zeidan et al. 2018). In brief, strains were cultured in YPD medium at 30°C to mid-logarithmic phase (OD_{600} of ~0.5-0.6). Fifteen A_{260} units of WCEs were resolved on a 10–50% sucrose gradient by centrifugation at 35,000 rpm. Gradients were fractionated with continuous scanning at 260 nm. Areas under the A_{260} tracings of polysome and monosome peaks were calculated using ImageJ software and used to calculate polysome to monosome (P/M) ratios in mutants and WT.

Ribosome footprint profiling

Duplicate cultures of yeast strains HFY114 (WT W303), SYY2352 (*scd6Δ*), FZY862 (*edc3Δ*), and FZY858 (*scd6Δedc3Δ*) were cultured in YPD medium at 30˚C to OD_{600} ~0.6-0.7. Yeast cells were quickly filtered, frozen in liquid nitrogen and stored at -80˚C. Cells were lysed in a freezer mill and ribosome protected mRNA fragments (RPF) were isolated and used for cDNA library preparation as described previously (Vijjamarri et al. 2023b). Single-end 100 bp Illumina sequencing was

performed by the National Heart, Lung and Blood Institute (NHLBI) DNA Sequencing and Genomics Core facility (Bethesda, MD).

RNA sequencing with spike-in normalization

The same lysates used for RPF library preparation were used to prepare RNA-Seq libraries after adding ERCC RNA Spike-In Control Mix 1 (Thermo Fisher Scientific, Cat. # 4456740). Total RNA was extracted from cell lysates using QIAzol Lysis reagent (Qiagen Cat. # 79306) and miRNeasy Mini Kit (Qiagen, Cat. 217004). Twenty µg of total RNA of each sample was subjected to RNase-free DNase I (Roche, Cat. # 04716728001) treatment and then processed with the RNA Clean and Concentrator Kit (Zymo, Cat. R1018). 2.4 µl of 1:100 diluted ERCC RNA Spike-In Control Mix 1 was added to 1.2 µg of each RNA sample and submitted to the NHLBI DNA Sequencing and Genomics Core facility (Bethesda, MD) for cDNA library preparation and Illumina sequencing.

Rpb1 ChIP-Seq with spike-in normalization

Triplicates of wild type and *scd6Δedc3Δ* yeast strains were cultured in rich YPD medium at 30˚C to OD600=0.6~0.8. Chromatin extracts were prepared from formaldehyde cross-linked cells as described previously (Qiu et al. 2016). *S. pombe* chromatin was added to each chromatin sample as a spike-in control prior to immunoprecipitation with Rpb1 antibodies, and ChIP-Seq DNA libraries were prepared as described previously (Zheng et al. 2023) subjected to 50 bp paired-

end Illumina sequencing by the NHLBI DNA Sequencing and Genomics Core facility (Bethesda, MD) and analyzed as previously described (Zheng et al. 2023).

Western blot analysis

For the results in Fig. 6B-C, WCEs were prepared by trichloroacetic acid (TCA) extraction as previously described (Reid and Schatz 1982) and immunoblot analysis was conducted as described previously (Nanda et al. 2009). After electroblotting to nitrocellulose membranes (Bio-Rad 1620094), membranes were probed with antibodies against Atp20, Cox14, Pet10, Qcr8, Sdh4 (kindly provided by Dr. Nikolaus Pfanner), Cyb2 (kindly provided by Dr. Thomas Fox), Idh1 (Abnova, PAB19472), Cit2 (Antibodies-online.com, ABIN4889057), and Gcd6 (Bushman et al. 1993). Secondary antibodies employed were HRP-conjugated anti-rabbit (Cytiva, NA9340V), anti-mouse IgG (Cytiva, NA931V) and anti-goat IgG (Abnova, PAB29101). Detection was performed using enhanced chemiluminescence (ECL) Western Blotting Detection Reagent (Cytiva, RPN2016) and the Azure 200 gel imaging biosystem. NIH Image J was employed to analyze images for quantification. For analysis of Cox2 levels in Fig. 6D, total proteins were TCA-extracted as described previously (Rashida et al. 2021) and subjected to Western blot analysis as recently described (Niphadkar et al. 2024) using mouse monoclonal antibody MTCO2 (4B12A5) from Invitrogen.

TMT-MS analysis of global protein abundance

TMT-MS analysis was conducted as described previously (Vijjamarri et al. 2023a) with the following modifications. Replicate cultures of WT, *edc3Δ, scd6Δ* and *scd6Δedc3Δ* strains were

cultured in YPD medium for ~3 doublings to OD_{600} of ~0.6, and harvested by centrifugation for 5 min at 3000 x *g.* Cells were resuspended in nuclease-free water, collected by centrifugation, and stored at -80°C. WCEs were prepared in freshly prepared 8M Urea, 25 mM triethylammonium-bicarbonate (TEAB; Thermo Scientific, 90114) by washing the cell pellets once and resuspending again in the extraction buffer, then vortexing with glass beads in the cold room. Lysates were clarified by centrifugation at 13,000 x *g* for 30 min and the quality of extracted proteins was assessed following SDS-PAGE using GelCode™ Blue Stain (Thermo Scientific, 24592) and quantified with the Pierce™ BCA Protein Assay Kit (Thermo Scientific, 23225). Lysates were stored at -80°C. Sample preparation, TMT-MS/MS (Zecha et al. 2019) and data analysis were performed at the IDeA National Resource for Quantitative Proteomics.

Measuring mitochondrial membrane potential

Precultures were grown in SC-Ura (to select for the *URA3* plasmids) to OD_{600} of ~3.0 and used to inoculate YPD medium at OD_{600} of 0.2. Cells were grown to OD_{600} of ~0.6-0.8, incubated with 500 nM TMRM for 1 h and subjected to flow cytometry to measure dye fluorescence in individual cells as described previously (Vijjamarri et al. 2023b). In control samples, 50 µM FCCP was added to dissipate the membrane potential and reveal non-specific background fluorescence. Results are presented in arbitrary fluorescence units normalized to OD_{600} of the cultures.

Analysis of polar metabolites of intermediary metabolism.

Yeast cell culturing. Four replicate 15 mL cultures in YEPD medium were prepared for each strain by inoculating with saturated overnight cultures to OD_{600} of 0.1, culturing with shaking at 30°C,

and harvesting at OD_{600} of 0.6 by centrifugation in conical 15mL tubes for 3 min at 3000 x g in an Avanti J-HC centrifuge pre-cooled to -10°C. Cell pellets were resuspended in 1.8 mL of ice-cold PBS and centrifuged in 2 mL screw-cap tubes in a refrigerated microfuge for 30 s. Supernatants were decanted, tube rims blotted on tissue paper, and cell pellets frozen in dry ice/ethanol for 5 min and stored at -80C. Frozen cell pellets were shipped on dry ice to the NYU Metabolomics Core Resource Laboratory.

Extraction of metabolites. Frozen cell pellets were thawed on wet ice. Extraction buffer, consisting of 80% methanol (Fisher Scientific) and 500 nM metabolomics amino acid mix standard (Cambridge Isotope Laboratories, Inc.), was prepared and placed on dry ice. Samples were extracted by mixing cell pellets with extraction buffer at 10mg/mL (determined by sample OD measurements) in 2.0 mL screw-cap vials containing ~100 µL of disruption beads (Research Products International, Mount Prospect, IL). Each sample was homogenized for 10 cycles on a bead blaster homogenizer (Benchmark Scientific, Edison, NJ), with each cycle consisting of 30 sec homogenization at 6 m/s followed by a 30 sec pause. Samples were centrifuged at 21,000 g for 3 min at 4°C. Aliquots of 450 µL were transferred to 1.5 mL tubes, dried in a Speedvac (Thermo Fisher, Waltham, MA), reconstituted in 50 µL of Optima LC/MS grade water (Fisher Scientific, Waltham, MA), sonicated for 2 min, and centrifuged at 21,000 g for 3 min at 4°C. Aliquots of 20 µL were transferred to LC vials containing glass inserts for analysis, and the remaining samples stored at -80°C.

LC-MS/MS with the hybrid metabolomics method. Samples were subjected to an LC-MS analysis to detect and quantify known peaks. Extraction of polar metabolites was carried out on each sample based on a previously described method (Jones et al. 2014). LC was conducted using a

Millipore™ ZIC-pHILIC (2.1 x150 mm, 5 µm) column coupled to a Dionex Ultimate 3000™ system with gradient elution conducted at 25°C with a flow rate of 100 µL/min using the following buffers A) 10 mM ammonium carbonate in water, pH 9.0, and B) neat acetonitrile. The gradient profile was as follows; 80-20% B (0-30 min), 20-80% B (30-31 min), 80-80% B (31-42 min). Injection volume was set to 2 µL for all analyses with a 42 min total run time per injection.

MS was conducted by coupling the LC system to a Thermo Q Exactive HF™ mass spectrometer operating in heated electrospray ionization mode (HESI). Method duration was 30 min with a polarity switching data-dependent Top 5 method for both positive and negative modes. Spray voltage for both positive and negative modes was 3.5kV and capillary temperature was set to 320 °C with a sheath gas rate of 35, aux gas of 10, and max spray current of 100 µA. The full MS scan for both polarities utilized 120,000 resolution with an AGC target of 3e6 and a maximum IT of 100 ms, and the scan range was from 67-1000 m/z. Tandem MS spectra for both positive and negative mode used a resolution of 15,000, AGC target of 1e5, maximum IT of 50 ms, isolation window of 0.4 m/z, isolation offset of 0.1 m/z, fixed first mass of 50 m/z, and 3-way multiplexed normalized collision energies (nCE) of 10, 35, 80. The minimum AGC target was 1e4 with an intensity threshold of 2e5. All data were acquired in profile mode.

Relative quantification and statistical analyses of polar metabolites. The resulting Thermo™ RAW files were converted to SQLite format using an in-house python script to enable downstream peak detection and quantification. The available MS/MS spectra were first searched against the NIST17 MS/MS (Simon-Manso et al. 2013), METLIN (Smith et al. 2005) and respective Decoy spectral library databases using an in-house data analysis python script adapted from our previously described approach for metabolite identification false discovery rate control (FDR)

(Wang et al. 2018; Wang et al. 2020). Metabolite peaks were extracted based on the theoretical m/z of the expected ion type, e.g., $[M+H]^+$, with a 15 part-per-million (ppm) tolerance and a ± 0.2 min peak apex retention time tolerance within an initial retention time search window of ±0.5 min. For all the group-wise comparisons, t-tests were performed using the Python SciPy (1.5.4) (Virtanen et al. 2020) library to test for differences and generate statistics for the downstream analyses. For the pairwise t-tests, any metabolite with a p-value < 0.01 was considered significantly regulated (up- or down-) for prioritization in the subsequent analyses.

Coverage of a library of polar metabolites of major pathways of intermediary metabolism allowed detection of 130 of the 147 metabolites examined in at least 4 samples, and 91 detected in all 20 samples after background threshold correction. Instrument performance was assessed using the internal standards added to the samples during metabolite extraction and instrument mass accuracy was within tolerance (-2.0 ppm), LC column performance was stable (0.16 min RT range) and internal standard response variability was 13% across the samples. The resulting data were analyzed by principal components analysis (Fig. 7A), by constructing heatmaps with unsupervised hierarchical clustering of the imputed matrix values utilizing the R library pheatmap (1.0.12). GraphPad Prism 9 (9.4.1, GraphPad Software, San Diego, CA), and volcano plots (generated utilizing R library script Manhattanly (0.2.0)), in addition to the statistical comparisons summarized in Supplementary File S7.

$^{13}C_6$-glucose metabolic flux measurements. Three replicate cultures of each strain were grown in YP medium with 2% unlabeled glucose to OD_{600} of 0.6-0.7 and then shifted to YP with 1% unlabeled glucose and cultured for 20 min. $^{13}C_6$-labelled glucose (1%) was then added and growth

was continued for 8 min. Cells were collected, and metabolites were extracted, derivatized and subjected to mass spectrometry as described previously, with the addition of additional masses for assessing the label incorporation into the specific labelled intermediates that were analyzed (Walvekar et al. 2018).

ATP Measurements

Cells were cultured in YPD to OD_{600} of 0.6-0.7 and treated or untreated with 5 mM sodium azide for 30 min at 30°C. Five OD_{600} units of cells were harvested and resuspended in 300 µL ice-cold 5% trichloroacetic acid (TCA), incubated on ice for 15 min, and diluted 50-fold in 20 mM Tris-HCl (pH 7.5) to 0.1 % TCA, after which 10 µL was mixed with 90 µL of ATP Determination reaction mixture (Cat. # A22066, Thermo-Fisher Scientific) and incubated at room temperature for 5 min. Units of Firefly Luciferase were measured in a Berthold Centro XS^3 LB 960 Luminometer, and ATP levels were calculated from an ATP standard curve generated using the same assay.

Additional data visualization and statistical analyses

Notched box-plots were constructed using a web-based tool at http://shiny.chemgrid.org/boxplotr/. In all such plots, the upper and lower boxes contain the 2nd and 3rd quartiles and the band gives the median. If the notches in two plots do not overlap, there is roughly 95% confidence that their medians differ. Density scatter plots, Venn diagrams, significance testing of gene set overlaps in Venn diagrams using the hypergeometric distribution, hierarchical clustering analysis, and gene ontology (GO) analysis all were conducted as described previously (Vijjamarri et al. 2023a).

RESULTS

Evidence that Scd6 and Edc3 functionally cooperate to control the abundance of many individual mRNAs. To determine whether Scd6 and Edc3 function redundantly in post-transcriptional control of gene expression, we constructed a *scd6Δedc3Δ* double mutant isogenic to the *scd6Δ* and *edc3Δ* single mutants we examined previously (Zeidan et al. 2018). Only the double mutant exhibits a marked slow-growth (Slg$^-$) phenotype on synthetic complete medium (SC), which was largely complemented by introducing either *SCD6* or *EDC3* on a single copy plasmid (Supplemental Fig. S1A). Analysis of polysome assembly revealed a ~40% reduction in ratio of polysomes to monosomes (P/M) in the *scd6Δedc3Δ* double mutant, whereas the single mutants showed little (*scd6Δ*) or no (*edc3Δ*) reduction in bulk translation by this assay (Fig. S1B). These results suggest that Scd6 and Edc3 function redundantly to carry out one or more functions required for WT levels of bulk translation and cell growth in nutrient replete cells.

To examine the effects of the *scd6Δ, edc3Δ,* and *scd6Δedc3Δ* mutations on the abundance and translation of individual mRNAs, we conducted RNA-Seq and ribosome profiling (Ribo-Seq) of the mutant and WT strains following growth in liquid rich medium (YPD) at 30°C (processed data compiled in supplementary File S1). Ribo-Seq entails deep-sequencing of ribosome-protected fragments (RPFs, or ribosome footprints), and cycloheximide was added to the lysates to arrest elongating ribosomes on the mRNA following cell breakage. The ratio of RPF sequencing reads summed over the coding sequences (CDS) to the total mRNA reads from RNA-Seq for the corresponding transcript provides a measure of translational efficiency (TE) for each mRNA (Ingolia et al. 2009). The ribosome profiling and RNA-Seq results between two biological

replicates for each strain were highly reproducible with Pearson correlation coefficients (r) ranging between 0.95-1.0 for different pairwise comparisons of replicates (Fig. S2A-B). We employed DESeq2 (Love et al. 2014) to identify statistically significant differences in relative mRNA abundance, RPF abundance, or TE for all expressed mRNAs between WT and mutant strains (see Methods for details).

Analysis of the RNA-Seq results identified 81 mRNAs that were significantly derepressed in the *edc3Δ* mutant vs. WT by >1.5-fold at a false discovery rate (FDR) of <0.05 (mRNA_up_e3; Fig. S3A), and 123 mRNAs reduced in abundance by *edc3Δ* by >1.5-fold at the same FDR (mRNA_dn_e3, Fig. S3B). Applying the same criteria, only 14 mRNAs were up-regulated and only 34 down-regulated by the *scd6Δ* single mutation (mRNA_up_s6 & mRNA_dn_s6, Fig. S3A-B). Importantly, much greater numbers of mRNAs were dysregulated by the *scd6Δedc3Δ* double mutation: 741 in the mRNA_up_s6,e3 group and 793 in the mRNA_dn_s6,e3 (Fig. S3A-B), indicating that the two factors have highly overlapping functions in controlling mRNA abundance with either one sufficient for nearly WT levels of most mRNAs dysregulated in the double mutant. *CIT1* mRNA, encoding a mitochondrial enzyme of the TCA cycle is representative of a transcript significantly up-regulated in both mRNA and RPF abundance only in the *scd6Δedc3Δ* double mutant (Fig. S3C).

Many yeast mutants with Slg$^-$ phenotypes, including *pat1Δ, dhh1Δ,* and *dcp2Δ* deletion mutants, exhibit altered expression of most mRNAs belonging to the Environmental Stress Response (ESR) (O'Duibhir et al. 2014), which includes ~300 induced (iESR) and ~600 repressed (rESR) mRNAs dysregulated in WT cells by various stresses (Gasch et al. 2000). In keeping with its Slg$^-$ phenotype, the *scd6Δedc3Δ* mutation conferred a marked reduction in median expression of

rESR mRNAs, and increased expression of the iESR mRNAs, which exceeded in magnitude the changes observed for the slowest growing yeast deletion mutants analyzed previously (O'Duibhir et al. 2014) (Fig. S3D-E). The two single mutations, by contrast, conferred much smaller changes in ESR mRNAs (Fig. S3D-E). (In all box plots, when notches do not overlap between adjacent boxes, their two medians differ with 95% confidence; and when notches do not overlap 0 in $\log_2$ plots, the median differs significantly from that of all mRNAs, which is invariably close to 1.0.) Consistent with these results, the transcripts up-regulated in the double mutant are enriched for iESR mRNAs (Fig. 1A), making it possible that the 187 iESR transcripts up-regulated in this strain are responding indirectly to cell stress. The remaining 75% of the mRNAs up-regulated in *scd6Δedc3Δ* cells are not iESR mRNAs however (Fig. 1A), suggesting that the increased abundance of these 554 transcripts arises from eliminating Edc3/Scd6 functions in mRNA decay. Below, we excluded the ESR mRNAs from analyses of mRNA changes in an effort to focus on mRNAs whose abundance is controlled directly by Scd6 and Edc3.

Considering only mRNAs not governed by the ESR, we identified 591 non-iESR mRNAs significantly up-regulated in any of the three mutants (Fig. 1B). Examining the ΔRNA values for the majority fraction of 521 transcripts up-regulated only in the double mutant confirms little change in median abundance in each single mutant and a strong synthetic derepression in the double mutant (Figs. 1B & 1C sector (iii))—as expected for redundant repressive functions of Scd6 and Edc3. *MDH2,* encoding an enzyme of the glyoxylate cycle, exemplifies a non-iESR transcript up-regulated in both mRNA and RPF abundance exclusively in the double mutant (Fig. 1D). The small fraction of 27 mRNAs significantly derepressed in both the *edc3Δ* single mutant and double mutant exhibits only slightly elevated median abundance in the *scd6Δ* single mutant, and only

slightly greater derepression in the double mutant vs. *edc3Δ* single mutant (Fig. 1B & 1C sector (ii)), indicating a minimal repressive contribution by Scd6. Interestingly, the small set of 37 mRNAs significantly derepressed only in the *edc3Δ* single mutant shows reduced rather than increased abundance in the *scd6Δ* single mutant, and lower derepression in the double mutant vs. the *edc3Δ* single mutant (Fig. 1B & C sector (i)), suggesting that Scd6 enhances rather than represses these mRNAs, especially in *edc3Δ* cells.

Evidence that Dhh1 and Pat1 functionally cooperate with Scd6/Edc3 in repressing mRNA abundance. We recently identified a large group of 1018 non-iESR mRNAs derepressed by either the *pat1Δ, dhh1Δ,* or *pat1Δdhh1Δ* mutations (Vijjamarri et al. 2023a). Importantly, this group is highly enriched for the 591 mRNAs derepressed by the *scd6Δ, edc3Δ,* or *scd6Δedc3Δ* mutations (Fig. 2A). Indeed, ~70% of the transcripts derepressed by *scd6Δ/edc3Δ* are also derepressed in one of the three *pat1Δ/dhh1Δ* mutants (Fig. 2A, sector (ii)), showing comparable up-regulation in the *scd6Δedc3Δ, pat1Δ,* and *dhh1Δ* mutants, but little change in the *scd6Δ* and *edc3Δ* single mutants (Fig. 2B(ii)). These mRNAs generally exhibit the greatest derepression in the *pat1Δdhh1Δ* double mutant, indicating cumulative contributions of Dhh1 and Pat1 to their repression, in contrast to the largely redundant roles played by Scd6 and Edc3 in repressing these mRNAs. Thus, efficient repression of these 411 mRNAs requires a combination of Pat1, Dhh1 and either Edc3 or Scd6. As expected, the smaller group of 180 mRNAs significantly derepressed exclusively by *scd6Δ/edc3Δ* (sector (i) of Fig. 2A) show strong derepression only in the *scd6Δedc3Δ* double mutant; but they are appreciably up-regulated by *dhh1Δ* while being largely unaffected by *pat1Δ* (Fig. 2B, sector (i)). Finally, the majority group of 607 mRNAs significantly derepressed by only

pat1Δ or *dhh1Δ* display the largest increases in the two mutants lacking Pat1, but display smaller and similar increases in response to the *scd6Δ/edc3Δ* and *dhh1Δ* mutations (Figs. 2A & 2B, sector (iii)). Overall, these findings suggest that Dhh1 and Pat1 both contribute to repressing the majority of mRNAs repressed by Scd6/Edc3, but with Dhh1 contributing more extensively than Pat1.

Further evidence for this last point comes from a k-means cluster analysis of mRNA changes in different mutants for the group of 431 non-iESR mRNAs derepressed by *dhh1Δ,* which revealed a stronger correlation between the changes conferred by *scd6Δ/edc3Δ* and *dhh1Δ* (ρ = 0.90) than between *pat1Δ* with either *dhh1Δ* (ρ = 0.74) or *scd6Δ/edc3Δ* (ρ = 0.71) (Fig. 2C). Consistent with this, the *scd6Δ/edc3Δ* mutations up-regulate a considerably larger proportion of the mRNAs significantly derepressed by *dhh1Δ* (~70%) vs. those derepressed by *pat1Δ* (~41%) (Fig. 2D). Furthermore, the majority of mRNAs up-regulated by *dhh1Δ* exhibit redundant repression by Scd6 and Edc3, showing marked derepression comparable to that given by *dhh1Δ* itself only in the *scd6Δ/edc3Δ* double mutant (Fig. 2E). These findings are consistent with the involvement of Edc3/Scd6 in the degradation of most mRNAs targeted by Dhh1, which are more variably and less extensively repressed by Pat1.

Evidence that Scd6/Edc3 repress mRNA abundance by enhancing decapping and degradation rather than suppressing transcription. We next examined whether the mRNAs significantly repressed by Edc3/Scd6 are also regulated by the decapping enzyme Dcp1/Dcp2. Supporting this, cluster analysis of mRNA changes revealed that the majority of non-iESR mRNAs derepressed in the *scd6Δedc3Δ* double mutant are also derepressed by *dcp2Δ* (Fig. 3A, blue colors in cols. 1 &

3), with a strong correlation between the abundance changes conferred by these mutations relative to WT (ρ=0.74, P≈0). In addition, *dcp2Δ* increased the median abundance of this group of mRNAs similarly to that given by *scd6Δedc3Δ* (Fig. 3B, cols. 1 & 4). These findings implicate decapping by Dcp1:Dcp2 as an important driver of the repression of mRNA levels directed by Scd6/Edc3. The cluster analysis in Fig. 3A once again reveals greater similarity between the mRNA changes conferred by *scd6Δedc3Δ* and those given by *dhh1Δ* (ρ = 0.90) versus *pat1Δ* (ρ = 0.69); and *pat1Δ* also confers a smaller median reduction than *dhh1Δ* of the Scd6/Edc3-repressed mRNAs (Fig. 3B).

Additional support for the conclusion that Scd6/Edc3 target mRNAs for decapping came from evidence that the mRNAs up-regulated in the *scd6Δedc3Δ* mutant tend to accumulate in WT cells as decapped isoforms. It is known that following decapping by Dcp1/Dcp2 mRNAs frequently undergo 5' to 3' decay co-translationally, with Xrn1 following behind the last translating ribosome loaded prior to decapping, and such decapped intermediates associated with ribosomes account for ~12% of the mRNAs in WT cells (Pelechano et al. 2015). We reasoned that mRNAs preferentially targeted by Scd6/Edc3 for decapping and attendant degradation by Xrn1 should exhibit a greater than average proportion of decapped intermediates in WT cells. To test this, we interrogated our previous cap analysis of gene expression (CAGE) data providing the abundance of all capped mRNA 5' ends and compared it to the abundance of total RNA transcripts determined by RNA-Seq conducted in parallel on biological replicates of mRNA samples prepared from the WT and *dhh1Δ* strains described above (Vijjamarri et al. 2023a). Transcript numbers per million reads (TPMs) from CAGE (C) and RNA-Seq (T) were determined and C/T ratios calculated as a proxy for the proportion of capped

molecules for each transcript (File S1). (Because the CAGE and RNA-Seq data were normalized separately, the C/T ratios are relative, not absolute, proportions of capped transcripts.) Importantly, the C/T ratios are lower in WT cells for the 448 non-iESR mRNAs up-regulated in the *scd6Δedc3Δ* double mutant (from Fig. 1B) compared to all expressed mRNAs for which CAGE data was obtained (Fig. 3C, cols. 1 & 5). By contrast, the C/T ratios are higher than average for the non-rESR mRNAs that are down-regulated in relative abundance in *scd6Δedc3Δ* cells, as expected for an unusually low degree of decapping in WT cells (Fig. 3C, cols 3 & 5). Importantly, these C/T ratios were elevated above their values in WT cells to nearly the same level for all groups of mRNAs, in the manner expected from eliminating Dhh1-stimulated decapping (Fig. 3C, cf. cols. 2,4,6). These results are consistent with the notion that impaired Dhh1-stimulated decapping and attendant 5' to 3' degradation is an important driver of increased mRNA abundance in the *scd6Δedc3Δ* mutant.

Independent evidence that derepression of mRNA abundance in *scd6Δedc3Δ* cells results from reduced decapping was provided by analyzing the codon protection indices (CPI) of the mRNA_up_s6,e3 transcripts, an indicator of co-translational decay by Xrn1. Decapped degradation intermediates exhibit three-nucleotide periodicity generated by precise Xrn1 cleavage up to the last translating ribosome at the 5' end of mRNA, and the CPI quantifies the prevalence of such intermediates for each mRNA (Pelechano et al. 2015). The results in Fig. 3D show that the mRNA_up_s6,e3 transcripts (including or excluding ESR mRNAs) exhibit higher than average median CPIs, indicating a greater than average involvement of decapping and co-translational degradation by Xrn1 in their decay, whereas mRNA_dn_s6,e3 transcripts exhibit

lower than average CPI values, consistent with an alternative degradation pathway controlling their abundance.

To determine whether increased transcription contributes to increased abundance of any mRNAs derepressed by *pat1Δ* or *dhh1Δ*, we performed ChIP-Seq analysis of Rpb1 to measure RNA Polymerase II (Pol II) occupancies averaged across the CDS of every gene. We obtained highly reproducible results for the three biological replicates analyzed for each strain (Fig. S2D & S4A). To quantify absolute changes in Pol II occupancies, *S. pombe* chromatin was added as a spike-in to each *S. cerevisiae* chromatin sample prior to immunoprecipitation of Rpb1. To measure absolute changes in mRNA abundance, we re-analyzed the RNA-Seq data taking into account the recovery of External RNA Controls Consortium (ERCC) transcripts that had been spiked-in prior to the replicate total RNA samples prior to preparation of the cDNA libraries. The results for ERCC-normalized RNA-Seq were highly reproducible among the replicates (Fig. S2C).

Considering all expressed mRNAs, the spike-in normalized RNA-Seq data (File S3) revealed a 46% increase in median total mRNA abundance in the *scd6Δedc3Δ* mutant vs. WT that was accompanied by only a 4% increase in median Rpb1 occupancy in the double mutant (Figs. 3E_alt, cols. 3 & 6), indicating that a reduced rate of mRNA decay associated with little change in transcription rate across the transcriptome leads to a net increase in total mRNA levels in the double mutant. Interrogating the two groups of non-ESR mRNAs found to be up- or down-regulated by *scd6Δedc3* revealed a 2.79-fold increase in spike-in normalized median mRNA abundance for the non-iESR mRNA_up_s6,e3 group that was associated with only a 1.2-fold increase in normalized Rpb1 occupancies, indicating a small contribution of increased transcription to the elevated mRNA abundance of these transcripts in the double mutant. The

down-regulated non-rESR mRNA_dn_s6,e3 transcripts showed 12% and 7% decreases in spike-in normalized median mRNA abundance and Rpb1 occupancies, respectively, indicating a larger contribution of transcriptional changes to the diminished transcript levels of these mRNAs in the double mutant. It should be noted that spike-in normalization of the RNA-Seq data reveals that the group of mRNAs up-regulated in the *scd6Δedc3Δ* mutant show larger increases in absolute compared to relative transcript levels (2.79-fold vs. 1.84-fold median increases) but show smaller absolute vs. relative reductions of the group of down-regulated transcripts (0.88-fold vs. 0.57-fold) (Fig. S4B, cf. cols. 1 vs. 4 and 2 vs. 5). This reflects the fact that the absolute changes conferred by *scd6Δedc3* for most transcripts involve the increased abundance expected from reduced decapping/decay in cells lacking Scd6/Edc3 (Fig. S4B, col. 3).

Codon nonoptimality has been linked with Dhh1-mediated mRNA decay partly by demonstrating that the sTAI values of mRNAs, which quantify their overall codon optimality (Sabi and Tuller 2014), are inversely correlated with the changes in mRNA abundance observed in *dhh1Δ* versus WT cells (Radhakrishnan et al. 2016). Similarly, analyzing the mRNA changes conferred by the *scd6Δedc3Δ* mutation for all non-ESR transcripts reveals a small but statistically significant negative correlation with sTAI values (Pearson r of -0.085, $P = 2 \times 10^{-9}$) similar to that observed for the *dhh1Δ* mutation ($r = -0.071$, $P = 6 \times 10^{-6}$) (Fig. S5A, cyan vs. orange), indicating a tendency for mRNAs with lower codon optimality/sTAI scores to show greater increases in relative abundance in response to *scd6Δedc3Δ* or *dhh1Δ*. However, the group of 591 non-iESR mRNAs most significantly up-regulated by the *scd6Δ/edc3Δ* mutations (from Fig. 1B) have a median sTAI value (0.35) nearly identical to that of all nonESR mRNAs, which is also the case for the group of 1018 mRNAs derepressed by the *pat1Δ* or *dhh1* mutations (Vijjamarri et al. 2023a)

(Fig. S5B). The same results were obtained for other metrics of codon optimality, tAI and average CSC (Fig. S5B), suggesting that poor codon optimality is not a key property defining the mRNAs repressed in abundance most extensively by these decapping activators in WT cells. It has also been proposed that competition between translation initiation and mRNA decay, rather than codon optimality and elongation, is a major determinant of mRNA stability in yeast (Muhlrad et al. 1995; LaGrandeur and Parker 1999; Schwartz and Parker 1999; Chan et al. 2018). However, the mRNAs derepressed in the *scd6Δ/edc3Δ* or *pat1Δ/dhh1* mutants have slightly greater than average median translational efficiencies (TEs) in WT cells (Fig. S5C), as determined by ribosome profiling experiments described below. Thus, mRNA features besides slow rates of translation initiation or elongation likely dictate preferential targeting by these four decapping activators.

Scd6 and Edc3 function redundantly and cooperate more extensively with Dhh1 than Pat1 in controlling the translation of individual mRNAs.

The changes in mRNA abundance were highly correlated with changes in RPF abundance for the *scd6Δedc3Δ* mutant compared to WT for all expressed transcripts, with an r value of 0.81 (Fig. S2F), providing strong mutual validation of the RNA-Seq and Ribo-Seq data for these strains. Nevertheless, the fact that this correlation is weaker than that observed between biological replicates of RNA-Seq or Ribo-Seq data for each strain (r values >0.95, Fig. S2A-B), suggests that certain mRNAs exhibit altered translational efficiencies in the double mutant. To identify specific mRNAs showing evidence of translational control by Scd6 and Edc3, we used DESeq2 to analyze our Ribo-Seq data on the *edc3Δ, scd6Δ* and *scd6Δedc3Δ* mutants, comparing each to WT. We identified 42 mRNAs showing TE increases of >1.41-fold at FDR < 0.10 in the *scd6Δ* mutant, but

only one such mRNA in the *edc3Δ* strain. Importantly, a larger number of mRNAs (N=184) were identified in the *scd6Δedc3Δ* double mutant (Fig. 4A), suggesting that Scd6 and Edc3 have overlapping functions in repressing the translation of particular mRNAs. Indeed, a group of 169 mRNAs that are translationally derepressed exclusively in the *scd6Δedc3Δ* double mutant (TE_up_s6,e3) exhibit only modest TE increases in the two single mutants compared to their marked derepression in the double mutant (Fig. 4A-B sector (iii)). *SPI1,* encoding a cell wall protein, is a representative transcript exhibiting increased TE only in the double mutant, displaying increased mRNA abundance coupled with an even greater increase in RPF abundance, both exclusively in the double mutant, to confer the observed TE increase of 3.2-fold (Fig. 4C). As expected, the 28 mRNAs showing substantial TE increases only in *scd6Δ* cells show no increase in median TE in the *edc3Δ* strain (Fig. 4A-B sector (i)), and thus appear to be translationally repressed by Scd6 alone.

We asked next whether the increased ribosome occupancies observed in the *scd6Δedc3Δ* double mutant are generally associated with increased synthesis of the encoded proteins. To this end, we carried out TMT mass spectrometry (TMT-MS) of total cellular proteins to obtain ratios of peptide abundance in the *scd6Δedc3Δ* double and WT strain mutant for >4000 different proteins, obtaining highly correlated results from three biological replicates (Fig. S2E). Importantly, we observed significant correlations between these changes in protein abundance and changes in ribosome occupancies (RPFs) for mRNAs across the translatome (Fig. 4D). Moreover, the groups of mRNAs showing significantly increased or decreased RPFs in the *scd6Δedc3Δ* double mutant vs. WT (>1.5-fold, FDR<0.05, Ribo_up and Ribo_dn) likewise exhibit increased or decreased median protein abundance determined by TMT-MS (Fig. 4E). These

results suggest that increased ribosome occupancies measured by Ribo-Seq, which could occur by increases in mRNA, TE, or both, are generally associated with increased synthesis of the encoded proteins in the *scd6Δedc3Δ* double mutant.

It was possible that translational repression by Edc3/Scd6 generally occurs by slowing the rate of elongation, leading to increased ribosome densities (RPF/mRNA ratios, ie. calculated TEs) in WT cells and decreased TE values in the *scd6Δedc3Δ* mutant that would be associated with increased protein expression in the mutant. In this scenario, changes in TEs would be inversely associated with changes in protein expression. At odds with this possibility, the groups of mRNAs showing increased or decreased TEs in the double mutant vs. WT (TE_up_s6,e3 and TE_dn_s6,e3 transcripts defined above) also exhibit increased or decreased protein expression in *scd6Δedc3Δ* vs. WT cells (Fig. 4F). These findings imply that Scd6/Edc3 generally influence translation at the level of initiation rather than elongation.

We previously identified a group of 274 mRNAs whose TEs are derepressed by the same criteria employed here (>1.41-fold at FDR < 0.10) in either the *pat1Δ, dhh1Δ,* or *pat1Δdhh1Δ* mutants versus WT (Vijjamarri et al. 2023a). Interestingly, we found a significant overlap between this group of mRNAs and those translationally derepressed in either the single or double *scd6Δ/edc3Δ* mutants identified here (Fig. 5A). The 76 mRNAs common to both groups show considerably larger TE increases in the *scd6Δedc3Δ* double mutant compared to the 136 transcripts whose TE was up-regulated only in the *scd6Δ/edc3Δ* mutants (Fig. 5A-B sector (ii) vs. sector (i)). The former 76 mRNAs also show marked TE increases in the *dhh1Δ, pat1Δ*, and *pat1Δdhh1Δ* mutants (Fig. 5B(ii)), indicating that all four decapping activators are required for efficient translational repression of these mRNAs in WT cells. The 136 mRNAs significantly

derepressed only in the *scd6Δ/edc3Δ* mutants show a moderate increase in median TE in *dhh1Δ* cells, but little response to *pat1Δ* (Fig. 5B(i)). The 198 mRNAs substantially derepressed only in the *pat1Δ/dhh1Δ* mutants show only a small TE increase in the *scd6Δedc3Δ* strain, a somewhat greater response to the *pat1Δ* vs. *dhh1Δ* single mutation, and cumulative TE increases in the *pat1Δdhh1Δ* double mutant (Fig. 5B(iii)). In summary, similar to our findings for repression of mRNA abundance, efficient translational repression of certain mRNAs requires the combined functions of Pat1, Dhh1, and either Scd6 or Edc3, whereas other mRNAs are translationally repressed primarily by either Edc3/Scd6 or Pat1, with appreciable contributions from Dhh1 for both of these latter groups.

Greater cooperation of Scd6/Edc3 with Dhh1 vs. Pat1 in controlling translation is also revealed by clustering analysis of TE changes in different mutants for the mRNAs exhibiting significantly increased or decreased TEs in the *scd6Δ/edc3Δ* mutants, which reveals a greater similarity between TE changes conferred by *scd6Δedc3Δ* vs. *dhh1Δ* (ρ = 0.82) compared to *scd6Δedc3Δ* vs. *pat1Δ* (ρ = 0.68) or *scd6Δedc3Δ* vs. *pat1Δdhh1Δ* (ρ = 0.69) cells (Fig. 5C). However, as noted above, the group showing the strongest derepression of TEs in the *scd6Δedc3Δ* double mutant also tends to be highly derepressed in all three of the other mutants lacking Dhh1 or Pat1 (bracketed mRNAs at the top of Fig. 5C). This behavior is illustrated in Fig. 5D for a group of 54 mRNAs whose TEs are derepressed by 2.0-fold or more in both the *scd6Δedc3Δ* and *pat1Δdhh1Δ* double mutants, displaying marked TE increases in the *scd6Δedc3Δ, pat1Δ, dhh1Δ,* and *pat1Δdhh1Δ* double mutants, but not in the *scd6Δ* and *edc3Δ* single mutants. Thus, although Scd6/Edc3 appear to cooperate more extensively with Dhh1 than with Pat1 in translational control, the subset of 50-60 mRNAs exhibiting the strongest repression by Scd6/Edc3 or

Pat1/Dhh1 require the concerted functions of Pat1, Dhh1, and either Scd6 or Edc3 to achieve their strong translational repression in WT cells.

We wondered whether the mRNAs translationally repressed by the decapping activators are also targeted for degradation by these factors. To assess this, we examined the mRNA changes in the four mutants for the groups of mRNAs defined above exhibiting TE derepression in the *scd6Δ/edc3Δ* or *pat1Δ/dhh1Δ* mutants (sectors (i) to (iii) of Fig. 5A). The group of mRNAs showing increased TEs only in the *pat1Δ/dhh1Δ* strains show little change in mRNA abundance in these mutants (Fig. S6A(iii)), indicating selective repression of translation vs degradation of these mRNAs. Similarly, the mRNAs translationally up-regulated only in the *scd6Δ/edc3Δ* mutants show little change in mRNA abundance in the *scd6Δedc3Δ* strain, while showing modest derepression in the *pat1Δ/dhh1Δ* mutants (Fig. S6A(i)). In contrast, the group of transcripts showing increased TEs in all of the mutants also show marked increases in mRNA abundance in all four mutants (Fig. S6A(ii)). Thus, coupled repression of translation and abundance by the decapping factors occurs only for the subset of transcripts exhibiting concerted translational repression by the four decapping activators. In contrast, the much larger groups of transcripts defined above showing increased mRNA abundance in the mutants (described in Fig. 2A) exhibit little change in median TE in all four mutants (Fig. S6B), suggesting that most mRNAs targeted for enhanced turnover do not exhibit translational repression of the fraction of undegraded transcripts still detectable in WT cells.

We next asked how well the mRNAs translationally repressed by Scd6/Edc3 are translated in WT cells. The group of mRNAs translationally repressed by Scd6/Edc3 acting in concert with Pat1/Dhh1 tend to be poorly translated in WT cells on rich medium, having a substantially lower

median relative TE compared to the TE of all mRNAs (0.24 vs. 0.95), as assessed using ribosome profiling results for the WT strain (Fig. S6C, col. 2), thus resembling the mRNAs translationally repressed exclusively by Dhh1/Pat1 (col. 3). In contrast, the subset of transcripts translationally repressed exclusively by Edc3/Scd6 are generally well translated, exhibiting a ~2.5-fold greater than average median TE in WT cells on rich medium (Fig. S6C, col. 1). Consistent with this distinction, we found by gene ontology (GO) analysis that products of the 136 mRNAs translationally repressed exclusively by Scd6/Edc3 are enriched for cytoplasmic or mitochondrial ribosomal proteins ($P = 1 \times 10^{-7}$), whereas products of the 76 transcripts repressed by Scd6/Edc3 and Pat1/Dhh1 acting in concert are enriched for factors involved in fermentation ($P = 2 \times 10^{-7}$), carbohydrate metabolism ($P = 1 \times 10^{-6}$) or metabolism of non-protein amino acids ($P = 3 \times 10^{-6}$). Thus, Scd6/Edc3 translationally repress distinct groups of mRNAs depending on whether Dhh1/Pat1 participate in the repression.

We showed previously (Zeidan et al. 2018) that mRNAs up-regulated by *dhh1Δ* and thus deemed to be targeted by Dhh1 for enhanced turnover are enriched for Dhh1 protein association in vivo as judged by RIP-Seq analysis of yeast mRNAs using antibodies against Dhh1 (Miller et al. 2018), thus providing evidence for a direct role of Dhh1 in stimulating decapping/degradation of these transcripts. The same was observed for the mRNAs up-regulated by *pat1Δ,* consistent with widespread cooperation between Dhh1 and Pat1 in repressing mRNA abundance (Vijjamarri et al. 2023a). Interestingly, here we observed greater than average Dhh1 occupancies for all four mRNA groups defined above (in Figs. 2A or 5A) that are up-regulated in transcript abundance or TE by the *scd6Δ/edc3Δ* or *dhh1Δ/pat1Δ* mutations (Fig. 5E). This finding is consistent with the fact that Dhh1 contributes to repressing the abundance or TE of the majority of transcripts in

these groups (Figs. 2B & 5B). It is possible that Dhh1 is recruited to nearly all of these mRNAs in a complex with Dcp1:Dcp2 and other decapping activators (He et al. 2022), but makes differential contributions to their degradation or translational repression.

Scd6/Edc3 repress post-transcriptionally repress mRNAs encoding enzymes of respiration and catabolism of non-glucose carbon sources in rich medium.

Recently, we reported that mRNAs up-regulated in abundance or TE in the *dcp2Δ, pat1Δ* and *dhh1Δ* mutants are enriched for mitochondrial proteins that function in Ox. Phos. (Vijjamarri et al. 2023a; Vijjamarri et al. 2023b). GO analysis led to the same finding here for the non-iESR mRNAs up-regulated in abundance by the *scd6Δ/edc3Δ* mutations, including many of the same categories of mitochondrial functions enriched among the mRNAs derepressed by the *dhh1Δ/pat1Δ* mutations (Fig. S7A-B, green entries). GO analysis of genes showing increased ribosome occupancies (RPFs), indicating either increased mRNA abundance or TE, confirms that the *scd6Δ/edc3Δ* mutations derepress the translation of Ox. Phos. gene transcripts (Fig. S7C-D). Examining a collection of Ox. Phos. genes functioning in electron transport, the TCA cycle or mitochondrial ATP synthase for changes in mRNA abundance, RPFs, and TEs reveals that the *scd6Δedc3Δ* and *pat1Δdhh1Δ* double mutations up-regulate expression of these genes primarily at the level of mRNA abundance, with small additional increases in TE (Fig. 6A). Western blot analysis revealed increased expression of four Ox. Phos. proteins (Qcr8, Atp20, Idh1, and Sdh4), two proteins (Cox14 and Cox20) involved in cytochrome c oxidase assembly, and mitochondrial cytochrome b2 (Cyb2) required for lactate utilization in *scd6Δedc3Δ* cells, relative to Gcd6 examined as loading control (Fig. 6B-C). Results similar to those in Fig. 6B-C were obtained for

the same set of mitochondrial proteins in the *dhh1Δ* and *pat1Δ* mutants (Vijjamarri et al. 2023a) and for a subset of these proteins in *dcp2Δ* cells (Vijjamarri et al. 2023b). Importantly, we also observed increased expression of Cox2, one of three mitochondrially encoded subunits of mitochondrial cytochrome *c* oxidase, terminal enzyme of the mitochondrial ETC, whose expression correlates well with mitochondrial activity (see https://elifesciences.org/reviewed-preprints/90293). Except for *dcp2Δ*, all the decapping mutants tested had significantly increased amounts of Cox2 protein (Fig 6D), suggesting an increase in ETC activity in these mutants. Derepression of mRNA and RPF abundance in *scd6Δedc3Δ* and *pat1Δdhh1Δ* double mutants also occurred for enzymes of the glyoxylate cycle (Fig. 6E), which catalyze certain reactions of the TCA cycle in the cytoplasm to support gluconeogenesis during respiratory growth on two-carbon compounds; and increased expression of one such enzyme, Cit2, was confirmed by Western analysis (Figs. 6B-C). Both Ox. Phos. and the glyoxylate cycle normally operate at low levels in yeast growing with abundant glucose, as in our experiments, suggesting that Scd6/Edc3 cooperate with Dhh1/Pat1 to help suppress these pathways in glucose-replete cells.

Consistent with post-transcriptional control of Ox. Phos. genes, the median relative RPF levels were up-regulated in the *scd6Δedc3Δ* mutant substantially more than the increases in relative Pol II occupancies observed at the cognate genes by ChIP-Seq analysis of Rpb1 (Fig. S8B, cols. 1-2). Moreover, the transcription factors responsible for induction of Ox. Phos. genes, the Hap2/Hap3/Hap4/Hap5 complex, were not activated in *scd6Δedc3Δ* cells: expression of a *CYC1-lacZ* reporter known to be activated by this Hap complex (Forsburg and Guarente 1989) was not elevated in the *scd6Δ/edc3Δ* mutants vs. WT in glucose-containing medium (Fig. 6F(ii)) but showed the expected induction in WT cells grown with glycerol/ethanol versus glucose (6F(i))

(Broach 2012). These findings support the notion that reduced decapping stabilizes Ox. Phos. gene transcripts in *scd6Δedc3Δ* cells.

In addition to Ox. Phos. genes, GO analysis revealed enrichment for genes involved in utilization of alternative carbon sources among those up-regulated at the level of mRNA or RPFs in the *scd6Δ/edc3Δ* mutants (Fig. S7A-D), as we observed recently for *dhh1Δ,pat1Δ* mutants (Vijjamarri et al. 2023a). Consistent with this, a group of 83 carbon catabolite repressed (CCR) genes, known to be glucose-repressed or activated by transcription factors Adr1 or Cat8 (Young et al. 2003; Tachibana et al. 2005), exhibit increased translation (RPFs) largely through increased mRNA abundance in both *scd6Δedc3Δ* and *pat1Δdhh1Δ* double mutants (Fig. S8A). This group includes enzymes for β-oxidation of fatty acids in addition to the glyoxylate cycle, which allow cells to synthesize precursors that can feed into gluconeogenesis or amino acid biosynthesis, or produce acetyl-CoA and generate NADH by respiration when growing on non-fermentable carbon sources (Young et al. 2003). The CCR genes exhibit larger increases in RPFs compared to Pol II occupancies at the cognate genes in *scd6Δedc3Δ* vs. WT cells (Fig. S8B, cols. 3-4), consistent with post-transcriptional repression of these genes by Scd6/Edc3. Supporting this, expression of an *ADH2-lacZ* reporter transcriptionally induced by activated Adr1 (Sloan et al. 1999) displayed the expected large induction in our WT strain cultured with glycerol/ethanol versus glucose as carbon source (Fig. S8C(i)), but its expression was actually reduced in the *scd6Δedc3Δ* mutant versus WT in glucose-grown cells (Fig. S8C(ii)).

Functional evidence that Scd6/Edc3 repress oxidative phosphorylation.

We examined the effects of eliminating Scd6/Edc3 on mitochondrial electron transport by measuring mitochondrial membrane potential ($\Delta\Psi_m$) generated by the ETC using the probe tetramethylrhodamine (TMRM)—a cationic fluorescent dye that accumulates in mitochondria as a function of $\Delta\Psi_m$. Quantifying dye fluorescence by flow cytometry revealed increased TMRM fluorescence in the *scd6Δedc3Δ* mutant containing an empty vector compared to both the isogenic WT strain and the mutant complemented by WT *EDC3* (Fig. 6G). These results are consistent with increased mitochondrial ETC activity in glucose-grown *scd6Δedc3Δ* cells.

To determine whether derepression of Ox. Phos. and other glucose-repressed genes in the decapping activator mutants alters cellular metabolites, we used targeted, quantitative LC-MS/MS based approaches (see Methods) to quantify levels of 147 polar metabolites in the isogenic *scd6Δedc3Δ*, *dhh1Δ, pat1Δ, dcp2Δ* and WT strains described above, cultured in YPD medium. Principle component analysis revealed clustering of results from biological replicates in the manner expected for reproducible differences in metabolite levels among different strains, with results for the *scd6Δedc3Δ* mutant most closely resemble those for *dhh1Δ,* which in turn were more similar to the results for *pat1Δ* vs. the *dcp2Δ* mutant or WT strains (Fig. 7A). This conclusion was borne out by cluster and correlation analyses of the changes in metabolites between each mutant compared to WT, with the strongest correlation observed for *scd6Δedc3Δ* vs. *dhh1Δ*, followed by *dhh1Δ* vs. *pat1Δ* (Fig. 7B). Considering the subset of 46 metabolites up-regulated in any two of the four mutants again showed greatest similarity between changes conferred by *scd6Δedc3Δ* vs. *dhh1Δ* followed by *dhh1Δ* vs. *pat1Δ* (Fig. 7C). These findings mirror the results from RNA-seq and ribosome profiling in which the up-regulation of mRNA levels or translation was most similar between the *scd6Δedc3Δ* and *dhh1Δ*

mutants. Pathway analysis of the 46 up-regulated metabolites (at https://www.metaboanalyst.ca/MetaboAnalyst/Secure/pathway) revealed a significant enrichment for metabolites of both the TCA and glyoxylate cycles (Fig. 7D), with five of six TCA cycle intermediates detected (fumarate, malate, α-ketoglutarate, cis-aconitate and citrate) being elevated in the decapping mutants (Fig. 7E). These results are consistent with the possibility that up-regulation of Ox. Phos. proteins (Fig. 6A-D) and ETC function (Fig. 6F) in the decapping mutants leads to increased flux from glucose towards the TCA cycle.

To determine unambiguously if there was indeed increased flux through the TCA cycle coming from glucose breakdown, we utilized a pulse label of $^{13}C_6$-glucose and then traced the ^{13}C label incorporation from glucose breakdown into intermediates of the TCA cycle. Specifically, WT and mutant cells were grown in high glucose, pulsed with $^{13}C_6$ glucose, and relative label incorporation into TCA cycle intermediates was estimated for each carbon molecule derived from glucose (as indicated schematically in Fig. 8A) eight min following the pulse. In all mutants, ^{13}C label incorporation in all TCA cycle intermediates was significantly higher than in WT cells (Fig. 8A), demonstrating that carbon flux from glucose into the TCA cycle was elevated in the decapping mutants. These results, along with increased ETC activity (Fig. 6G), indicate that mitochondria are functionally derepressed in glucose in these mutants. If so, we might expect the mutants to show increased ATP production from respiration versus glycolysis. Measuring total ATP levels in glucose-grown cells revealed that, although all of the decapping mutants except *pat1Δ* showed some reduction in total levels of ATP per cell (Fig. 8B), the proportion of ATP produced from respiration, and thus eliminated by sodium azide treatment (by inhibiting the ETC), is elevated in all of the decapping mutants (Fig. 8C).

Interestingly, amino acids are also up-regulated in the decapping mutants (Fig. 7D), particularly in *pat1Δ* cells (Fig. 7F), as well as intermediates in amino acid biosynthesis and amino acid derivatives (Fig. 7D). The expression of amino acid biosynthetic enzymes is unaffected or reduced in the mutants however (Fig. S8D), suggesting that increased amino acid abundance results from metabolic reprogramming rather than increased biosynthetic capacity. One possibility is that accumulation of the TCA cycle intermediate α-ketoglutarate leads to increased production of glutamate and glutamine, which are precursors in all amino acid biosynthetic pathways (Ljungdahl and Daignan-Fornier 2012). The two 3-phosphotrioses generated in glycolysis (glyceraldehyde 3-phosphate and dihydroxyacetone phosphate) are also elevated in the mutants, possibly owing to increased glyoxylate shunt function, which can lead to precursors of these intermediates and stimulate synthesis of amino acids serine and glycine (Ljungdahl and Daignan-Fornier 2012) (Fig. 7D, Methane metabolism category. The increases in fructose 1,6-bisphosphate, fructose 6-phosphate, glucose 6-phosphate, and UDP-glucose in all four mutants (Fig. 7D, Starch/Sucrose metabolism category) all suggest substantial metabolic rewiring indicative of glucose derepression and usage of alternative carbon sources. In addition to amino acids, pyrimidine nucleotides are up-regulated in the mutants (Fig. 7D, Pyrimidine metab.), which might be driven by the elevated glutamine levels or increased glycolytic flux towards the pentose phosphate pathway (Ljungdahl and Daignan-Fornier 2012).

DISCUSSION

RNA-seq analysis of single and double *scd6Δ* and *edc3Δ* mutants has revealed that Scd6 and Edc3 have largely overlapping functions in repressing mRNA abundance, as the presence of

either protein alone is sufficient for nearly WT levels of most mRNAs found derepressed in the double mutant (Fig. S3A & Fig. 1B-C(ii)-(iii)). The mRNAs dysregulated in the *scd6Δedc3Δ* mutant are significantly enriched for ESR mRNAs; however, the majority are not ESR transcripts and are most likely repressed more directly by Scd6/Edc3 (Fig. 1A-B). Scd6/Edc3 redundancy in regulating mRNA abundance is consistent with their similarities in sequence and domain structure, including shared FDF motifs that interact competitively with Dhh1 (Tritschler et al. 2008; Tritschler et al. 2009) and N-terminal LSm domains that compete for binding motifs in the Dcp2 CTT (Fromm et al. 2012), as well as the synthetic growth defect produced by deleting both genes simultaneously (Decourty et al. 2008) (Fig. S1A). Interestingly, a set of 37 mRNAs appears to be repressed exclusively by Edc3 with little contribution from Scd6, or with even an opposing stimulatory effect of Scd6, on their abundance (Fig. 1B-C(i)). This last group includes the canonical Edc3 targets identified previously, *YRA1* and *RPS28B* (He et al. 2022) and, interestingly, is enriched for genes belonging to the GO category "mitochondrion" (22/37 genes) and the Ox. Phos. categories of electron transport and mitochondrial ATP synthesis (11/37 genes: *ATP3 ATP16 ATP5 TIM11 ATP17 COX4 QCR9 CYC1 COX12 ATP18 COX5A*). The fact that deleting *SCD6* in the double mutant frequently diminishes the up-regulation of these transcripts conferred by deleting *EDC3* alone (Fig. 1C(i)) might indicate that eliminating both Scd6 and Edc3 together enables a distinct degradation pathway that compensates for loss of Edc3-stimulated decapping/decay.

Several lines of evidence support the conclusion that most of the changes in mRNA abundance in the *scd6Δedc3Δ* double mutant result from impaired decapping and attendant 5'-3' degradation by Xrn1. ChIP-seq analysis of Rpb1 shows that Pol II occupancies in the coding sequences increase by a much smaller amount compared to the increased transcript levels for

non-iESR mRNAs derepressed in *scd6Δ/edc3Δ* cells (Fig. 3E), indicating a minor contribution of increased transcription to their up-regulation. Consistent with mRNA turnover via decapping, most of these transcripts are up-regulated similarly by *scd6Δedc3Δ* and deletion of *DCP2* (Fig. 3A-B), they exhibit a heightened proportion of decapped isoforms in WT cells that is eliminated by deleting *DHH1* (Fig. 3C), and they show evidence of co-translational 5'-3' decay of decapped intermediates by Xrn1 (Fig. 3D); none of which was observed for the mRNAs down-regulated in *scd6Δ/edc3Δ* cells. Similar findings were reported previously for sets of mRNAs up-regulated by *dhh1Δ* or *pat1Δ* (Vijjamarri et al. 2023a), consistent with the widespread involvement of Dhh1 and Pat1 in controlling the levels of mRNAs preferentially targeted by Scd6/Edc3.

Supporting this last assertion, most (~70%) of the mRNAs repressed in abundance by Edc3/Scd6 are also repressed by Dhh1 and Pat1, and their efficient repression in WT cells involves independent contributions of similar magnitude by Pat1, Dhh1 and either Edc3 or Scd6 (Fig. 2A-B(ii)). Another large set of mRNAs is repressed predominantly by Pat1 with lesser comparable contributions by Dhh1 and Scd6/Edc3 (Fig. 2A-B(iii)). Our finding of extensive cooperation among these four decapping factors in repressing a common set of mRNAs is consistent with our recent finding that ~55% of the mRNAs derepressed in the *dcp2Δ* mutant, and thus targeted by Dcp2 for enhanced degradation, tend to be derepressed in the *pat1Δdhh1Δ* and *scd6Δedc3Δ* mutants, whereas the remaining 45% are generally derepressed by *upf1Δ* instead. This finding suggested a major bifurcation of Dcp2-activation by either Pat1/Dhh1/Scd6/Edc3 or the Upf factors responsible for NMD (Vijjamarri et al. 2023b).

Closer examination of the effects of individual mutations on mRNA levels revealed a greater overlap between the mRNAs dysregulated by *dhh1Δ* and *scd6Δ/edc3Δ* versus those

altered by *pat1Δ* (Fig. 2C-E), consistent with the aforementioned FDF motifs in both Scd6 and Edc3 that interact with Dhh1, and with evidence for distinct complexes of the decapping enzyme Dcp1:Dcp2 containing Dhh1 and Edc3 or Scd6 but lacking Pat1. It also supports the recent suggestion that Edc3 and Scd6 act interchangeably to recruit Dhh1 to the Edc3-interaction site in the Dcp2 CTT to stimulate turnover of several Dhh1 target mRNAs (He et al. 2022). Our RNA-seq results support this last proposal in revealing that all four Dhh1 target mRNAs examined there (*EDC1, SDS23, HXT6,* and *HSP12*) are derepressed in the *scd6Δedc3Δ* double mutant while showing little derepression in either single mutant (Fig. S9), as expected for redundant targeting of Dhh1 to the Dcp2-CTT by Scd6/Edc3. Finding here that this behavior applies to most mRNAs up-regulated in the *dhh1Δ* mutant (Fig. 2E), we propose that redundant Scd6/Edc3 targeting is the predominant mechanism of Dhh1-enhanced mRNA degradation in the yeast transcriptome (Fig. S10).

Despite strong evidence for the involvement of decapping in mRNA turnover directed by either Scd6/Edc3 or Pat1/Dhh1, it appears that neither enrichment for non-optimal codons nor low translational efficiencies are principal determinants of preferential targeting of mRNAs by these proteins (Fig. S5A-B). There are probably exceptions to these generalizations among the hundreds of transcripts repressed by these factors; nor can we rule out the involvement of clusters of non-optimal codons in transcripts of average overall codon optimality that generate a queue of slowly elongating ribosomes that triggers decapping. Nevertheless, it seems likely that other sequences or properties of the transcripts most strongly repressed by Scd6/Edc3 or Dhh1/Pat1 frequently underlie their preferential targeting by these factors for decapping/decay. Sequence-specific RNA-binding proteins that actively recruit these decapping activators is an

attractive potential mechanism (Fig. S10). For example, there is evidence that Dhh1 is recruited to mRNAs in association with the Ccr4-NOT deadenylase via RNA-binding protein Puf5 (Goldstrohm et al. 2006).

Ribosome profiling of the single and double *scd6Δ* and *edc3Δ* mutants provided evidence that Scd6 and Edc3 also have highly overlapping functions in repressing the translation of ~200 mRNAs, whose TE values are up-regulated substantially only in the double mutant (Fig. 4A-B(iii)). The observation that changes in TE (RPF density) generally correlate with changes in protein abundance conferred by *scd6Δedc3Δ* (Fig. 4E) implies that Scd6/Edc3 generally repress translation at the stage of initiation rather than elongation. Many mRNAs translationally repressed by Scd6/Edc3 additionally require Dhh1, and the subset most strongly repressed also requires Pat1 for efficient translational repression (Fig. 5B(ii) and 5D). This last group of mRNAs is translated at very low levels in WT cells on rich medium (Fig. S6C), which might reflect the concerted action of all four decapping activators in suppressing their translation. The transcript abundance of these mRNAs is also derepressed in each of the mutants (Fig. S6A(ii)), indicating enhanced degradation coupled with translational repression by the four decapping activators. One possibility is that a complex of Dcp1:Dcp2 containing Scd6/Edc3, Pat1/Dhh1, or different combinations of these factors (He et al. 2022), is recruited to these mRNAs and impedes recruitment of PICs to diminish translation in parallel with stimulating decapping and 5'-3' degradation by Xrn1 (Fig. S10(i) & (ii)-(iv)).

The additional sets of mRNAs identified here that are translationally repressed exclusively by Scd6/Edc3 or Pat1/Dhh1 (Fig. 5A(i) & (iii)) show much less evidence of transcript degradation promoted by these factors (Fig. S6A(i) & (iii)), suggesting that inhibition of PIC recruitment for

translation initiation occurs without decapping, or that it involves decapping uncoupled from degradation by Xrn1 (Fig. S10 (ii)-(iii)). In the latter scenario, the decapped mRNAs would be unable to recruit the cap-binding initiation factors necessary for PIC recruitment and hence persist in WT cells as translationally-inert degradation intermediates. Eliminating the decapping activators would then diminish decapping and eliminate these fractions of poorly translated transcript isoforms to confer the increased TE values we observed for the cognate genes in the decapping mutants. This hypothetical mechanism of translational repression via decapping is consistent with the lower than average capped to total mRNA (C/T) ratios observed in WT cells for the mRNAs translationally repressed by all four decapping activators or by Pat1/Dhh1 (Fig. S6D (ii)-(iii)), indicating their high rates of decapping and accumulation of decapped isoforms in WT cells. Previously, we suggested that such translational repression via decapping could account for a subset of poorly translated mRNAs exhibiting TE increases in both *dcp2Δ* and *dhh1Δ* mutants and showing Dhh1-dependent lower than average C/T ratios in WT (Vijjamarri et al. 2023b). In contrast, the group of mRNAs identified here that are translationally repressed exclusively by Scd6/Edc3 display higher than average C/T ratios in WT (Fig. S6D(i)), which is more compatible with the inhibition of PIC recruitment independently of decapping (Fig. S10(iii)). Translational repression without decapping or decay could also occur if transcripts bound by the decapping complexes are sequestered from the translation initiation machinery in RNA granules in a state where mRNA decapping or degradation by Xrn1 occurs inefficiently (Fig S9(iv)). Finally, it is important to note that mRNA decay occurs apparently without translational control for the much larger groups of ~600 and ~1000 transcripts showing derepressed mRNA abundance but little evidence of TE changes in the *scd6Δedc3Δ* and *pat1Δdhh1Δ* mutants, respectively (Fig. S6B). It is

unclear whether these mRNAs escape translational repression and are targeted exclusively for decapping and degradation (Fig. S10(i)), or if they are simply degraded too fast to allow translational repression to be detected by ribosomal profiling of steady-state mRNAs.

Recently, we reported that Pat1 and Dhh1 functionally collaborate with the decapping enzyme to repress genes and cellular pathways that are normally repressed in rich medium (Vijjamarri et al. 2023a; Vijjamarri et al. 2023b). Here we found evidence that Scd6 and Edc3 broadly cooperate with Pat1/Dhh1 in this post-transcriptional control, acting redundantly to down-regulate the abundance, translation, or both, of mRNAs encoding numerous proteins involved in respiration or utilization of alternative carbon sources (Figs. 6A-C, S6C, S7A-B), without affecting transcription of the cognate genes Fig. 6F, S7A-C). This derepression includes multiple nucleus-encoded mitochondrial proteins that function in Ox. Phos. (Fig. S7C-D & Fig. 6A-B), including mitochondrially encoded subunit II of ETC component cytochrome *c* oxidase (Fig. 6D). Evidence that derepression of Ox. Phos. mRNAs/proteins in the *scd6Δedc3Δ* mutant is sufficient to elevate respiration in glucose-replete cells came from our finding of elevated mitochondrial membrane potential in the *scd6Δedc3Δ* mutant, extending similar findings we made previously for *dcp2Δ, dhh1Δ* and *pat1Δ* mutants (Vijjamarri et al. 2023a; Vijjamarri et al. 2023b). Consistent with this, our metabolomics analysis here revealed elevated steady-state levels of TCA cycle intermediates in all four decapping mutants (Fig. 7D), and metabolic flux experiments on cells pulse-labeled with $^{13}C_6$-glucose demonstrated increased carbon incorporation from glucose breakdown into TCA cycle intermediates in the same mutant strains (Fig. 8A). Analysis of ATP levels further revealed increased proportions of ATP derived from Ox. Phos. in the decapping mutants (Fig. 8B). Together, these findings provide strong evidence that

mitochondrial respiration is inappropriately elevated in glucose-replete cells of the decapping activator mutants. It is well established that the enzymes involved in respiration and catabolism of non-glucose carbon sources are repressed at the transcriptional level in glucose-replete yeast (Zaman et al. 2008). Our findings demonstrate that Scd6/Edc3 collaborate with Dhh1/Pat1 to provide an additional layer of post-transcriptional control of these enzymes through enhanced decapping/decay or translational repression to help ensure their complete suppression in glucose-replete cells.

DATA AVAILABILITY

Ribosome profiling, RNA-Seq, ChIP-Seq and CAGE-Seq data discussed in this publication have been deposited in NCBI's Gene Expression Omnibus and are accessible through GEO Series accession numbers GSE270789 and GSE270790. TMT-MS/MS proteomics raw data have been deposited in ProteomeXchange with accession number PXD053307. Previously published datasets used in this study can be found in (Vijjamarri et al. 2023a; Vijjamarri et al. 2023b).

ACKNOWLEDGEMENTS

We are grateful to Drew Jones, Tori Rodrick and the NYU Langone Medical Metabolomics Lab for valuable advice, metabolomics data acquisition and analysis, Samuel Mackintosh and IDeA National Resource for Quantitative Proteomics for TMT-MS analysis, and the NHLBI DNA Sequencing and Genomics Core for all next-generation DNA sequencing. We thank Feng He and Allan Jacobson and Bertrand Séraphin for gifts of yeast strains, Nikolaus Pfanner and Thomas Fox for gifts of antibodies, and Henry Zhang for help with bioinformatics.

We are grateful to Jon Lorsch for financial support of DNA sequencing and invaluable advice, and all other members of our laboratories for helpful comments and suggestions. This work was supported in part by the Intramural Research Program of the NIH. C.O. and M.L.G. were supported by NIH grants R01 HL117880 and R35 GM149271, and SL acknowledges support from a DBT-Wellcome Trust India Alliance Senior Fellowship IA/S/21/2/505922.

REFERENCES

Arribere JA, Doudna JA, Gilbert WV. 2011. Reconsidering movement of eukaryotic mRNAs between polysomes and P bodies. *Mol Cell* **44**: 745-758.

Badis G, Saveanu C, Fromont-Racine M, Jacquier A. 2004. Targeted mRNA degradation by deadenylation-independent decapping. *Mol Cell* **15**: 5-15.

Broach JR. 2012. Nutritional control of growth and development in yeast. *Genetics* **192**: 73-105.

Buschauer R, Matsuo Y, Sugiyama T, Chen YH, Alhusaini N, Sweet T, Ikeuchi K, Cheng J, Matsuki Y, Nobuta R et al. 2020. The Ccr4-Not complex monitors the translating ribosome for codon optimality. *Science* **368**.

Bushman JL, Asuru AI, Matts RL, Hinnebusch AG. 1993. Evidence that GCD6 and GCD7, translational regulators of *GCN4* are subunits of the guanine nucleotide exchange factor for eIF-2 in *Saccharomyces cerevisiae*. *Mol Cell Biol* **13**: 1920-1932.

Carroll JS, Munchel SE, Weis K. 2011. The DExD/H box ATPase Dhh1 functions in translational repression, mRNA decay, and processing body dynamics. *J Cell Biol* **194**: 527-537.

Celik A, Baker R, He F, Jacobson A. 2017. High-resolution profiling of NMD targets in yeast reveals translational fidelity as a basis for substrate selection. *RNA* **23**: 735-748.

Chan LY, Mugler CF, Heinrich S, Vallotton P, Weis K. 2018. Non-invasive measurement of mRNA decay reveals translation initiation as the major determinant of mRNA stability. *Elife* **7**.

Coller J, Parker R. 2005. General translational repression by activators of mRNA decapping. *Cell* **122**: 875-886.

Decourty L, Saveanu C, Zemam K, Hantraye F, Frachon E, Rousselle JC, Fromont-Racine M, Jacquier A. 2008. Linking functionally related genes by sensitive and quantitative characterization of genetic interaction profiles. *Proc Natl Acad Sci U S A* **105**: 5821-5826.

Dong S, Li C, Zenklusen D, Singer RH, Jacobson A, He F. 2007. YRA1 autoregulation requires nuclear export and cytoplasmic Edc3p-mediated degradation of its pre-mRNA. *Mol Cell* **25**: 559-573.

Forsburg SL, Guarente L. 1989. Identification and characterization of HAP4: a third component of the CCAAT-bound HAP2/HAP3 heteromer. *Genes Dev* **3**: 1166-1178.

Fromm SA, Truffault V, Kamenz J, Braun JE, Hoffmann NA, Izaurralde E, Sprangers R. 2012. The structural basis of Edc3- and Scd6-mediated activation of the Dcp1:Dcp2 mRNA decapping complex. *EMBO J* **31**: 279-290.

Gasch AP, Spellman PT, Kao CM, Carmel-Harel O, Eisen MB, Storz G, Botstein D, Brown PO. 2000. Genomic expression programs in the response of yeast cells to environmental changes. *Mol Biol Cell* **11**: 4241-4257.

Goldstein AL, McCusker JH. 1999. Three new dominant drug resistance cassettes for gene disruption in Saccharomyces cerevisiae. *Yeast* **15**: 1541-1553.

Goldstrohm AC, Hook BA, Seay DJ, Wickens M. 2006. PUF proteins bind Pop2p to regulate messenger RNAs. *Nat Struct Mol Biol* **13**: 533-539.

He F, Celik A, Wu C, Jacobson A. 2018. General decapping activators target different subsets of inefficiently translated mRNAs. *Elife* **7**.

He F, Jacobson A. 2015. Control of mRNA decapping by positive and negative regulatory elements in the Dcp2 C-terminal domain. *RNA* **21**: 1633-1647.

-. 2023. Eukaryotic mRNA decapping factors: molecular mechanisms and activity. *FEBS J* **290**: 5057-5085.

He F, Li X, Spatrick P, Casillo R, Dong S, Jacobson A. 2003. Genome-wide analysis of mRNAs regulated by the nonsense-mediated and 5' to 3' mRNA decay pathways in yeast. *Mol Cell* **12**: 1439-1452.

He F, Wu C, Jacobson A. 2022. Dcp2 C-terminal cis-binding elements control selective targeting of the decapping enzyme by forming distinct decapping complexes. *Elife* **11**.

Holmes LE, Campbell SG, De Long SK, Sachs AB, Ashe MP. 2004. Loss of translational control in yeast compromised for the major mRNA decay pathway. *Mol Cell Biol* **24**: 2998-3010.

Hu G, McQuiston T, Bernard A, Park YD, Qiu J, Vural A, Zhang N, Waterman SR, Blewett NH, Myers TG et al. 2015. A conserved mechanism of TOR-dependent RCK-mediated mRNA degradation regulates autophagy. *Nat Cell Biol* **17**: 930-942.

Ingolia NT, Ghaemmaghami S, Newman JR, Weissman JS. 2009. Genome-wide analysis in vivo of translation with nucleotide resolution using ribosome profiling. *Science* **324**: 218-223.

Jones DR, Wu Z, Chauhan D, Anderson KC, Peng J. 2014. A nano ultra-performance liquid chromatography-high resolution mass spectrometry approach for global metabolomic profiling and case study on drug-resistant multiple myeloma. *Anal Chem* **86**: 3667-3675.

Jungfleisch J, Nedialkova DD, Dotu I, Sloan KE, Martinez-Bosch N, Bruning L, Raineri E, Navarro P, Bohnsack MT, Leidel SA et al. 2017. A novel translational control mechanism involving RNA structures within coding sequences. *Genome Res* **27**: 95-106.

LaGrandeur T, Parker R. 1999. The cis acting sequences responsible for the differential decay of the unstable MFA2 and stable PGK1 transcripts in yeast include the context of the translational start codon. *Rna* **5**: 420-433.

Ljungdahl PO, Daignan-Fornier B. 2012. Regulation of amino acid, nucleotide, and phosphate metabolism in Saccharomyces cerevisiae. *Genetics* **190**: 885-929.

Love MI, Huber W, Anders S. 2014. Moderated estimation of fold change and dispersion for RNA-seq data with DESeq2. *Genome Biol* **15**: 550.

Miller JE, Zhang L, Jiang H, Li Y, Pugh BF, Reese JC. 2018. Genome-Wide Mapping of Decay Factor-mRNA Interactions in Yeast Identifies Nutrient-Responsive Transcripts as Targets of the Deadenylase Ccr4. *G3 (Bethesda)* **8**: 315-330.

Muhlrad D, Decker CJ, Parker R. 1995. Turnover mechanisms of the stable yeast PGK1 mRNA. *Mol Cell Biol* **15**: 2145-2156.

Nanda JS, Cheung YN, Takacs JE, Martin-Marcos P, Saini AK, Hinnebusch AG, Lorsch JR. 2009. eIF1 controls multiple steps in start codon recognition during eukaryotic translation initiation. *J Mol Biol* **394**: 268-285.

Niphadkar S, Karinje L, Laxman S. 2024. The PP2A-like phosphatase Ppg1 mediates assembly of the Far complex to balance gluconeogenic outputs and enables adaptation to glucose depletion. *PLoS Genet* **20**: e1011202.

Nissan T, Rajyaguru P, She M, Song H, Parker R. 2010. Decapping activators in Saccharomyces cerevisiae act by multiple mechanisms. *Mol Cell* **39**: 773-783.

O'Duibhir E, Lijnzaad P, Benschop JJ, Lenstra TL, van Leenen D, Groot Koerkamp MJ, Margaritis T, Brok MO, Kemmeren P, Holstege FC. 2014. Cell cycle population effects in perturbation studies. *Mol Syst Biol* **10**: 732.

Paquette DR, Tibble RW, Daifuku TS, Gross JD. 2018. Control of mRNA decapping by autoinhibition. *Nucleic Acids Res* **46**: 6318-6329.

Parker R. 2012. RNA degradation in Saccharomyces cerevisae. *Genetics* **191**: 671-702.

Pelechano V, Wei W, Steinmetz LM. 2015. Widespread Co-translational RNA Decay Reveals Ribosome Dynamics. *Cell* **161**: 1400-1412.

Presnyak V, Alhusaini N, Chen YH, Martin S, Morris N, Kline N, Olson S, Weinberg D, Baker KE, Graveley BR et al. 2015. Codon optimality is a major determinant of mRNA stability. *Cell* **160**: 1111-1124.

Qiu H, Chereji RV, Hu C, Cole HA, Rawal Y, Clark DJ, Hinnebusch AG. 2016. Genome-wide cooperation by HAT Gcn5, remodeler SWI/SNF, and chaperone Ydj1 in promoter nucleosome eviction and transcriptional activation. *Genome Res* **26**: 211-225.

Radhakrishnan A, Chen YH, Martin S, Alhusaini N, Green R, Coller J. 2016. The DEAD-Box Protein Dhh1p Couples mRNA Decay and Translation by Monitoring Codon Optimality. *Cell* **167**: 122-132 e129.

Rashida Z, Srinivasan R, Cyanam M, Laxman S. 2021. Kog1/Raptor mediates metabolic rewiring during nutrient limitation by controlling SNF1/AMPK activity. *Sci Adv* **7**.

Reid GA, Schatz G. 1982. Import of proteins into mitochondria. Yeast cells grown in the presence of carbonyl cyanide m-chlorophenylhydrazone accumulate massive amounts of some mitochondrial precursor polypeptides. *J Biol Chem* **257**: 13056-13061.

Sabi R, Tuller T. 2014. Modelling the efficiency of codon-tRNA interactions based on codon usage bias. *DNA Res* **21**: 511-526.

Schwartz DC, Parker R. 1999. Mutations in translation initiation factors lead to increased rates of deadenylation and decapping of mRNAs in Saccharomyces cerevisiae. *Mol Cell Biol* **19**: 5247-5256.

Sharif H, Ozgur S, Sharma K, Basquin C, Urlaub H, Conti E. 2013. Structural analysis of the yeast Dhh1-Pat1 complex reveals how Dhh1 engages Pat1, Edc3 and RNA in mutually exclusive interactions. *Nucleic Acids Res* **41**: 8377-8390.

Simon-Manso Y, Lowenthal MS, Kilpatrick LE, Sampson ML, Telu KH, Rudnick PA, Mallard WG, Bearden DW, Schock TB, Tchekhovskoi DV et al. 2013. Metabolite profiling of a NIST Standard Reference Material for human plasma (SRM 1950): GC-MS, LC-MS, NMR, and clinical laboratory analyses, libraries, and web-based resources. *Anal Chem* **85**: 11725-11731.

Sloan JS, Dombek KM, Young ET. 1999. Post-translational regulation of Adr1 activity is mediated by its DNA binding domain. *J Biol Chem* **274**: 37575-37582.

Smith CA, O'Maille G, Want EJ, Qin C, Trauger SA, Brandon TR, Custodio DE, Abagyan R, Siuzdak G. 2005. METLIN: a metabolite mass spectral database. *Ther Drug Monit* **27**: 747-751.

Sweet T, Kovalak C, Coller J. 2012. The DEAD-Box Protein Dhh1 Promotes Decapping by Slowing Ribosome Movement. *PLoS Biol* **10**: e1001342.

Tachibana C, Yoo JY, Tagne JB, Kacherovsky N, Lee TI, Young ET. 2005. Combined global localization analysis and transcriptome data identify genes that are directly coregulated by Adr1 and Cat8. *Mol Cell Biol* **25**: 2138-2146.

Tritschler F, Braun JE, Eulalio A, Truffault V, Izaurralde E, Weichenrieder O. 2009. Structural basis for the mutually exclusive anchoring of P body components EDC3 and Tral to the DEAD box protein DDX6/Me31B. *Mol Cell* **33**: 661-668.

Tritschler F, Eulalio A, Helms S, Schmidt S, Coles M, Weichenrieder O, Izaurralde E, Truffault V. 2008. Similar modes of interaction enable Trailer Hitch and EDC3 to associate with DCP1 and Me31B in distinct protein complexes. *Mol Cell Biol* **28**: 6695-6708.

Vijjamarri AK, Gupta N, Onu C, Niu X, Zhang F, Kumar R, Lin Z, Greenberg ML, Hinnebusch AG. 2023a. mRNA decapping activators Pat1 and Dhh1 regulate transcript abundance and translation to tune cellular responses to nutrient availability. *Nucleic Acids Res*.

Vijjamarri AK, Niu X, Vandermeulen MD, Onu C, Zhang F, Qiu H, Gupta N, Gaikwad S, Greenberg ML, Cullen PJ et al. 2023b. Decapping factor Dcp2 controls mRNA abundance and translation to adjust metabolism and filamentation to nutrient availability. *Elife* **12**.

Virtanen P, Gommers R, Oliphant TE, Haberland M, Reddy T, Cournapeau D, Burovski E, Peterson P, Weckesser W, Bright J et al. 2020. SciPy 1.0: fundamental algorithms for scientific computing in Python. *Nat Methods* **17**: 261-272.

Walvekar A, Rashida Z, Maddali H, Laxman S. 2018. A versatile LC-MS/MS approach for comprehensive, quantitative analysis of central metabolic pathways. *Wellcome Open Res* **3**: 122.

Wang X, Cho JH, Poudel S, Li Y, Jones DR, Shaw TI, Tan H, Xie B, Peng J. 2020. JUMPm: A Tool for Large-Scale Identification of Metabolites in Untargeted Metabolomics. *Metabolites* **10**.

Wang X, Jones DR, Shaw TI, Cho JH, Wang Y, Tan H, Xie B, Zhou S, Li Y, Peng J. 2018. Target-Decoy-Based False Discovery Rate Estimation for Large-Scale Metabolite Identification. *J Proteome Res* **17**: 2328-2334.

Webster MW, Chen YH, Stowell JAW, Alhusaini N, Sweet T, Graveley BR, Coller J, Passmore LA. 2018. mRNA Deadenylation Is Coupled to Translation Rates by the Differential Activities of Ccr4-Not Nucleases. *Mol Cell* **70**: 1089-1100 e1088.

Young ET, Dombek KM, Tachibana C, Ideker T. 2003. Multiple pathways are co-regulated by the protein kinase Snf1 and the transcription factors Adr1 and Cat8. *J Biol Chem* **278**: 26146-26158.

Zaman S, Lippman SI, Zhao X, Broach JR. 2008. How Saccharomyces responds to nutrients. *Annu Rev Genet* **42**: 27-81.

Zecha J, Satpathy S, Kanashova T, Avanessian SC, Kane MH, Clauser KR, Mertins P, Carr SA, Kuster B. 2019. TMT Labeling for the Masses: A Robust and Cost-efficient, In-solution Labeling Approach. *Mol Cell Proteomics* **18**: 1468-1478.

Zeidan Q, He F, Zhang F, Zhang H, Jacobson A, Hinnebusch AG. 2018. Conserved mRNA-granule component Scd6 targets Dhh1 to repress translation initiation and activates Dcp2-mediated mRNA decay in vivo. *PLoS Genet* **14**: e1007806.

Zheng Q, Qiu H, Zhang H, Hinnebusch AG. 2023. Differential requirements for Gcn5 and NuA4 HAT activities in the starvation-induced versus basal transcriptomes. *Nucleic Acids Res* **51**: 3696-3721.

FIGURES & LEGENDS

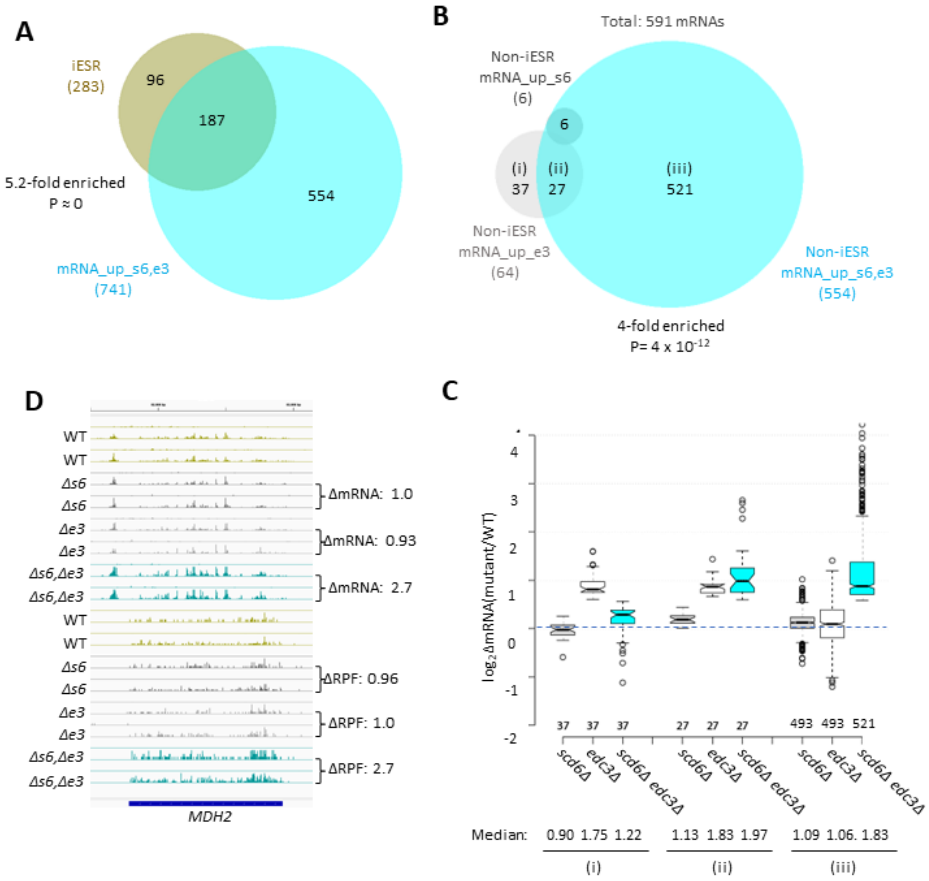

Fig. 1. Most mRNAs up-regulated in the *scd6Δedc3Δ* mutant are not iESR transcripts and exhibit Scd6/Edc3 functional redundancy in repression of transcript abundance. (A) Venn diagram of overlap between the 741 mRNAs up-regulated in the *scd6Δedc3Δ* mutant vs. WT and the 283 induced ESR mRNAs, indicating fold-enrichment and P value of overlap determined by the hypergeometric distribution. **(B)** Venn diagram of overlaps involving all 591 non-iESR mRNAs derepressed in abundance by either the *scd6Δ, edc3Δ*, or *scd6Δedc3Δ* mutations. **(C)** Notched box-plot analyses of $\log_2$ changes in mRNA abundance ($\log_2$ΔmRNA) determined by DESeq2 analysis between the indicated mutants vs. WT for mRNAs belonging to the specified sectors of

the Venn diagram in (B). Un-logged median values are indicated at the bottom. **(D)** Gene browser image for *MDH2* presented as in Fig. S3C.

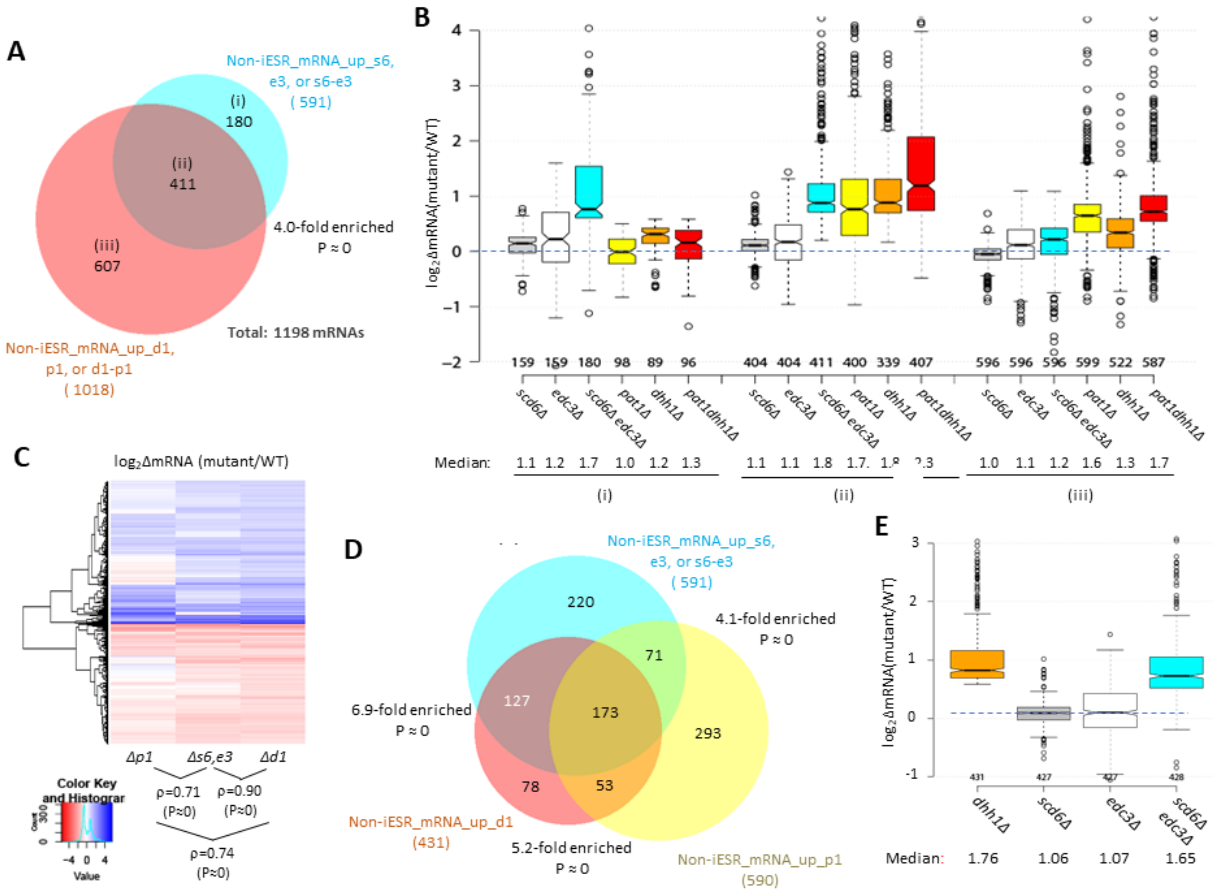

Fig. 2. Most mRNAs up-regulated in the *scd6Δedc3Δ* mutant are also derepressed by *dhh1Δ* and *pat1Δ*. (A) Venn diagram of overlap between all 591 non-iESR mRNAs derepressed in abundance by the *scd6Δ, edc3Δ*, or *scd6Δedc3Δ* mutations (from Fig. 1B) and 1018 non-iESR mRNAs up-regulated by the *dhh1Δ, pat1Δ*, or *pat1Δdhh1Δ* mutations identified previously (Vijjamarri et al. 2023a). **(B)** Notched box-plots of $\log_2$ΔmRNA between the indicated mutants vs. WT for mRNAs in the three sectors specified in (A). **(C)** Hierarchical clustering analysis of $\log_2$ΔmRNA values conferred by the indicated mutations vs. WT for 784 of the 794 mRNAs up- or down-regulated in *dhh1Δ* vs. WT cells for which RNA-Seq data was obtained in all four strains and with $\log_2$ΔmRNA values >-5 and <5, conducted with R heatmap.2 function from R 'gplots' library, using default

hclust hierarchical clustering algorithm. Spearman coefficients (ρ) and associated P values are given for the indicated correlation analyses. **(D)** Venn diagram of overlaps between the 591 non-iESR mRNAs up-regulated by the *scd6Δ/edc3Δ* mutations vs. WT (from Fig. 1B) and the indicated 431 and 590 non-iESR mRNAs up-regulated by *dhh1Δ* or *pat1Δ* vs. WT, respectively, identified previously (Vijjamarri et al. 2023a). **(E)** Notched box-plots of $\log_2$ΔmRNA between the indicated mutants vs. WT for the 431 non-iESR mRNAs up-regulated by *dhh1Δ* vs. WT shown in panel (D).

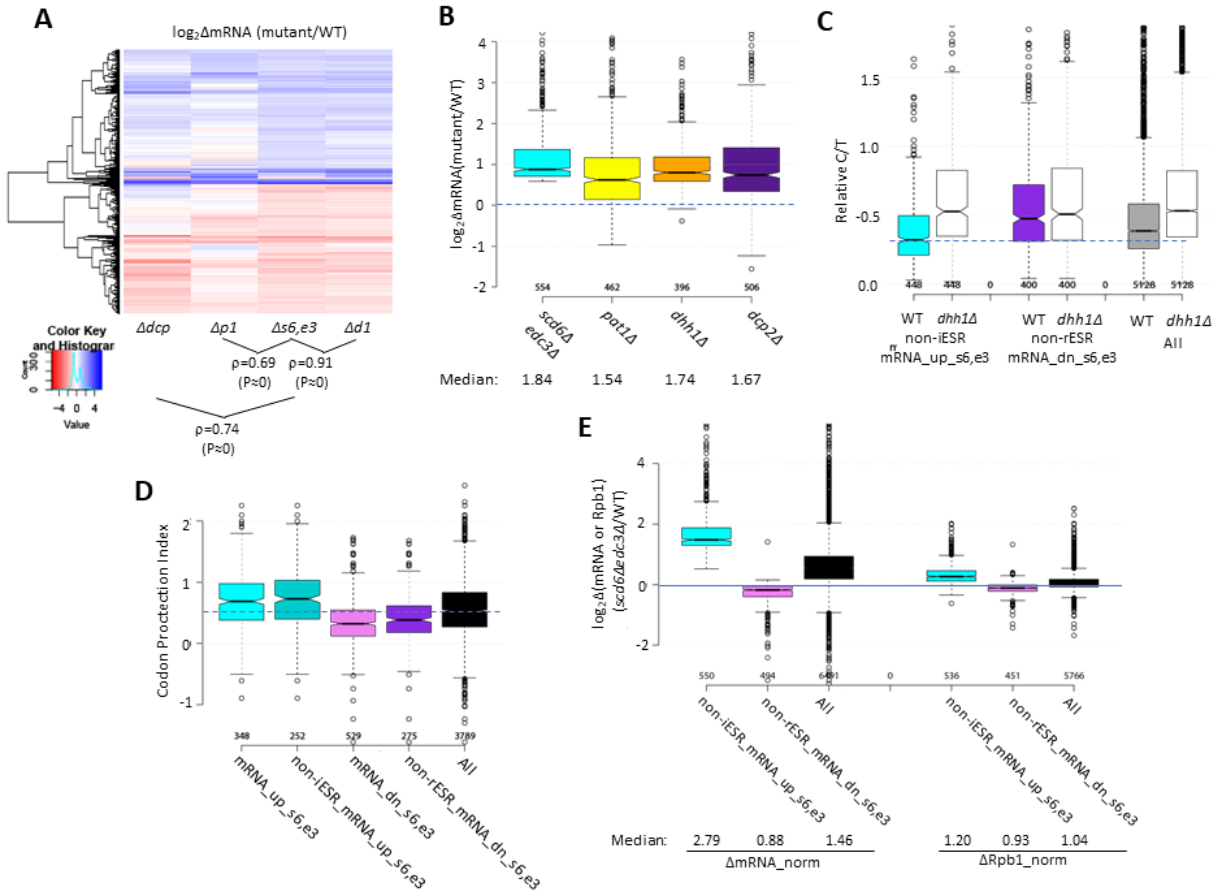

Fig. 3. Evidence that impaired decapping rather than increased transcription is a key driver of changes in mRNA abundance in *scd6Δedc3Δ* cells. (A) Hierarchical clustering analysis of $\log_2$ΔmRNA values conferred by the indicated mutations vs. WT for 741 of the 1052 mRNAs up- or down-regulated in *scd6Δedc3Δ* vs. WT cells for which RNA-Seq data was obtained in all five strains and with $\log_2$ΔmRNA values >-5 and <5, conducted as in Fig. 2C, showing Spearman coefficients and P values for indicated correlations. **(B)** Notched box-plots of $\log_2$ΔmRNA between the indicated mutants vs. WT for the 554 non-iESR mRNAs up-regulated by *scd6Δedc3Δ* vs. WT (shown in Fig. 1B). **(C)** Ratios of capped to total mRNA abundance in TPMs (Relative C/T) in WT or *dhh1Δ* cells plotted for all mRNAs or the 554 non-iESR mRNA_ up_s6,e3 or 526 non-rESR

mRNA_down_s6,e3 transcripts dysregulated by *scd6Δedc3Δ* vs. WT. **(D)** Notched box-plots of the codon-protection index (CPI) for all mRNAs or for the sets of mRNAs up- or down-regulated by *scd6Δedc3Δ* vs. WT, including or excluding ESR transcripts, as indicated. **(E)** Notched box-plots showing $\log_2$ changes in absolute mRNA abundance from ERCC spike-in normalized RNA-Seq (left) or absolute Rpb1 occupancies averaged over the CDSs from *S. pombe* chromatin spike-in normalized Rpb1 ChIP-Seq (right) in *scd6Δedc3Δ* vs. WT cells for all mRNAs or the 554 or 526 non-ESR mRNAs up- or down-regulated, respectively, by *scd6Δedc3Δ* vs. WT.

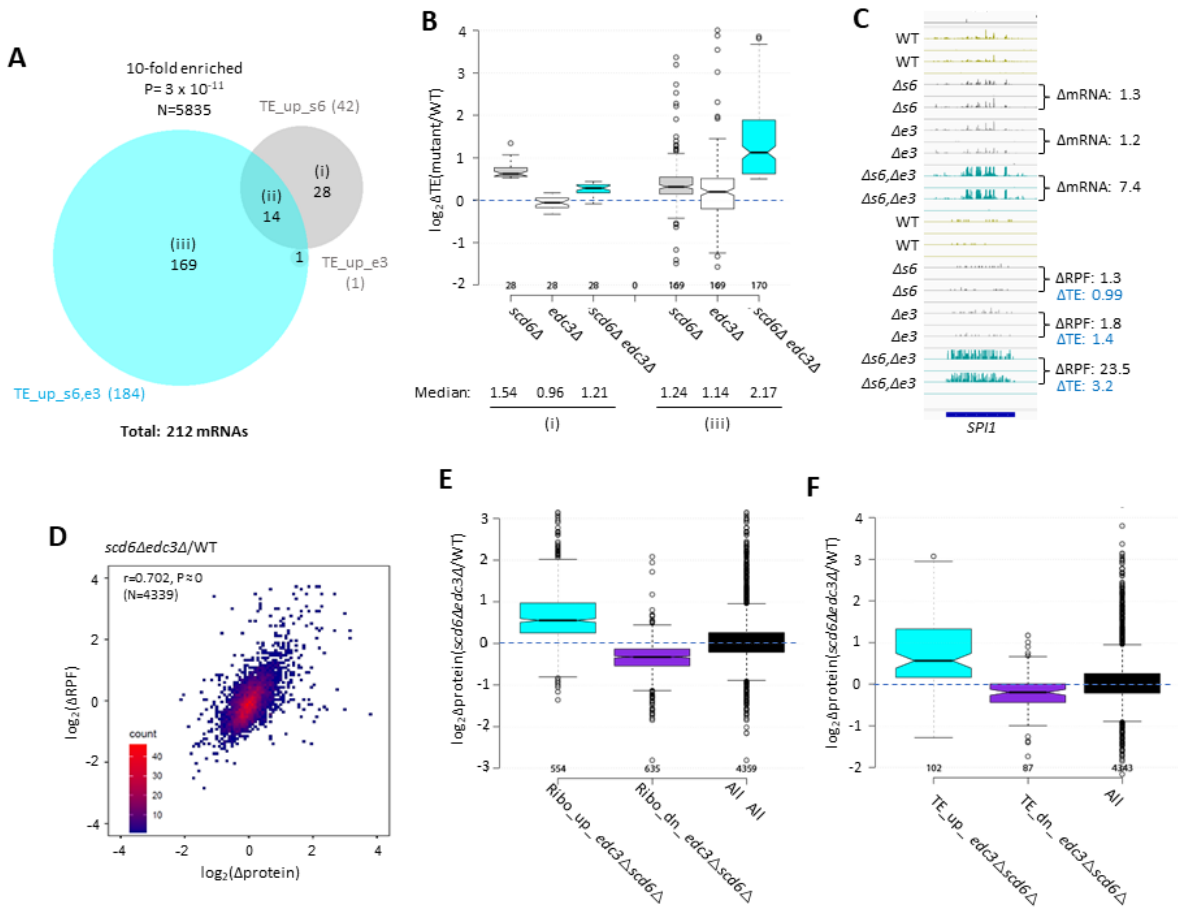

Fig. 4. Most mRNAs translationally up-regulated in *scd6Δedc3Δ* cells exhibit Scd6/Edc3 functional redundancy for repressing TE and show correlated changes in TE and protein abundance. (A) Venn diagram of overlap between the 184 and 42 mRNAs in the TE_up groups identified in the *scd6Δedc3Δ* vs. WT or *scd6Δ* vs. WT comparisons, respectively. **(B)** Notched box-plots of $\log_2\Delta$TE values between the indicated mutants vs. WT for the mRNAs belonging to sectors (i) or (iii) of the diagram in (A). **(C)** Gene browser image for *SPI1* presented as in Fig. S3C, except also giving the TE changes for each mutant vs. WT on the lower right. **(D)** Density scatterplot of $\log_2\Delta$RPF values measured by ribosome profiling vs. $\log_2\Delta$protein values measured by TMT-MS for 4339 mRNAs for which data were obtained in both analyses, indicating the Pearson correlation coefficient (r) and P-value of the correlation. **(E-F)** Notched box-plots of $\log_2\Delta$protein

values from TMT-MS analysis between the *scd6Δedc3Δ* mutant vs. WT for the 843 and 839 mRNAs belonging to the RPF_up or RPF_down groups, respectively (D), or the 184 and 152 TE_up or TE_down mRNA groups (E) determined for the *scd6Δedc3Δ* mutant vs. WT, or for all mRNAs, for which TMT-MS data was obtained.

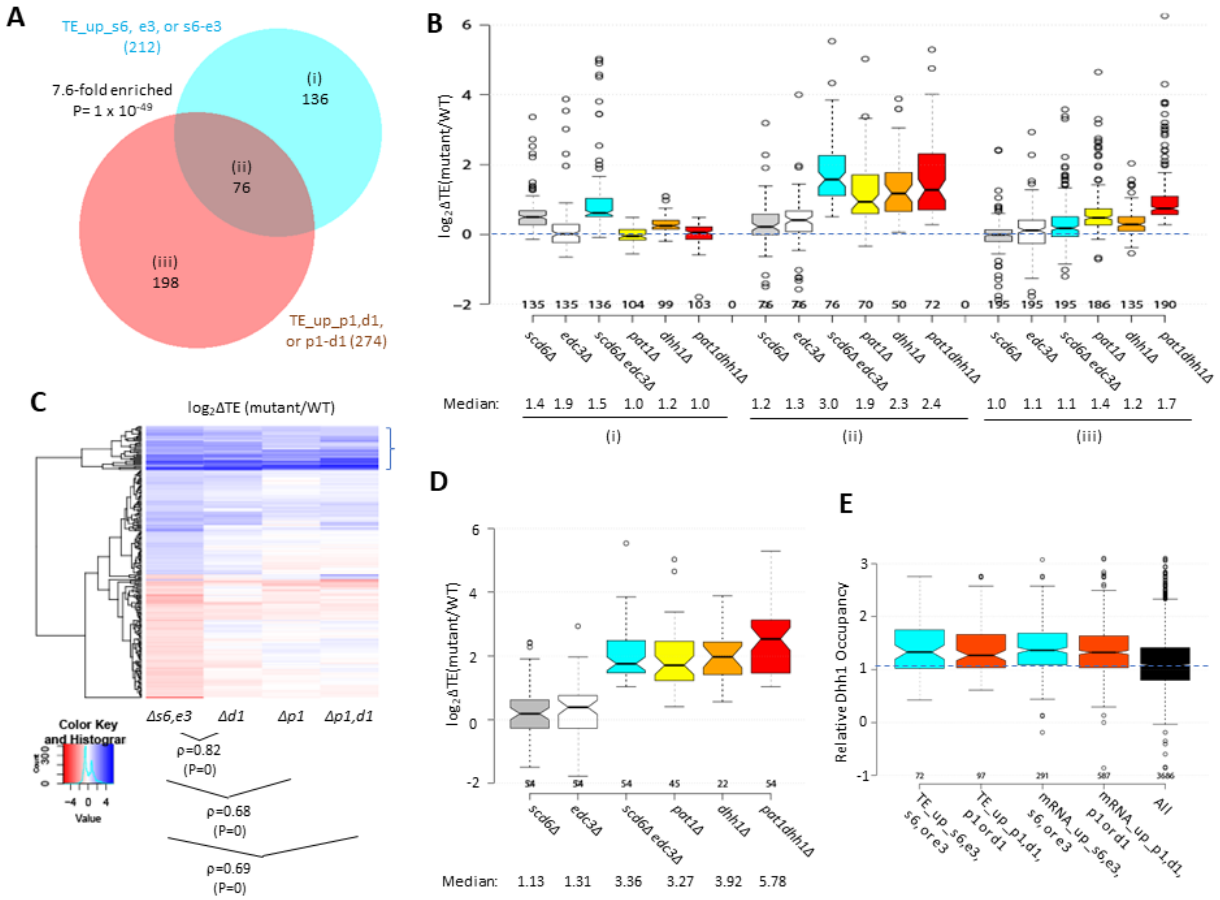

Fig. 5. Most mRNAs translationally up-regulated in the *scd6Δedc3Δ* mutant are also translationally derepressed by *dhh1Δ* or *pat1Δ*. (A) Venn diagram of overlap between all 212 mRNAs translationally derepressed by *scd6Δ, edc3Δ*, or *scd6Δedc3Δ* (defined in Fig. 4A) or all 274 mRNAs translationally derepressed by *dhh1Δ, pat1Δ*, or *pat1Δdhh1Δ* vs. WT identified previously (Vijjamarri et al. 2023a). **(B)** Notched box-plots of $\log_2\Delta TE$ values between the indicated mutants vs. WT for the mRNAs belonging to the specified sectors of the diagram in (A). **(C)** Hierarchical clustering analysis of $\log_2\Delta TE$ values conferred by the indicated mutations vs. WT for 222 of the 336 mRNAs translationally up- or down-regulated in *scd6Δedc3Δ* vs. WT cells for which RNA-Seq and Ribo-Seq data were obtained in all five strains and with $\log_2\Delta TE$ values >-5 and <5 conducted as in Fig. 2C, including the Spearman coefficients (ρ) and P values

for the indicated correlations. **(D)** Notched box-plots of $\log_2\Delta$TE values between the indicated mutants vs. WT for the 54 mRNAs showing >2-fold TE increases conferred by both *scd6Δedc3Δ* and *pat1Δdhh1Δ* mutations vs. WT. **(E)** Relative Dhh1 occupancies from the Dhh1 RIP-seq experiments of Miller et al (2018) for the 212 and 274 mRNAs identified as TE_up in the *scd6Δ, edc3Δ*, or *scd6Δedc3Δ* mutants, or the *dhh1Δ, pat1Δ*, or *pat1Δdhh1Δ* mutants, vs. WT, respectively (cols 1-2), or for the 591 and 1018 mRNAs identified as mRNA_up in either the *scd6Δ, edc3Δ*, or *scd6Δedc3Δ* mutants, or the *dhh1Δ, pat1Δ*, or *pat1Δdhh1Δ* mutants, vs. WT, respectively (cols. 3-4).

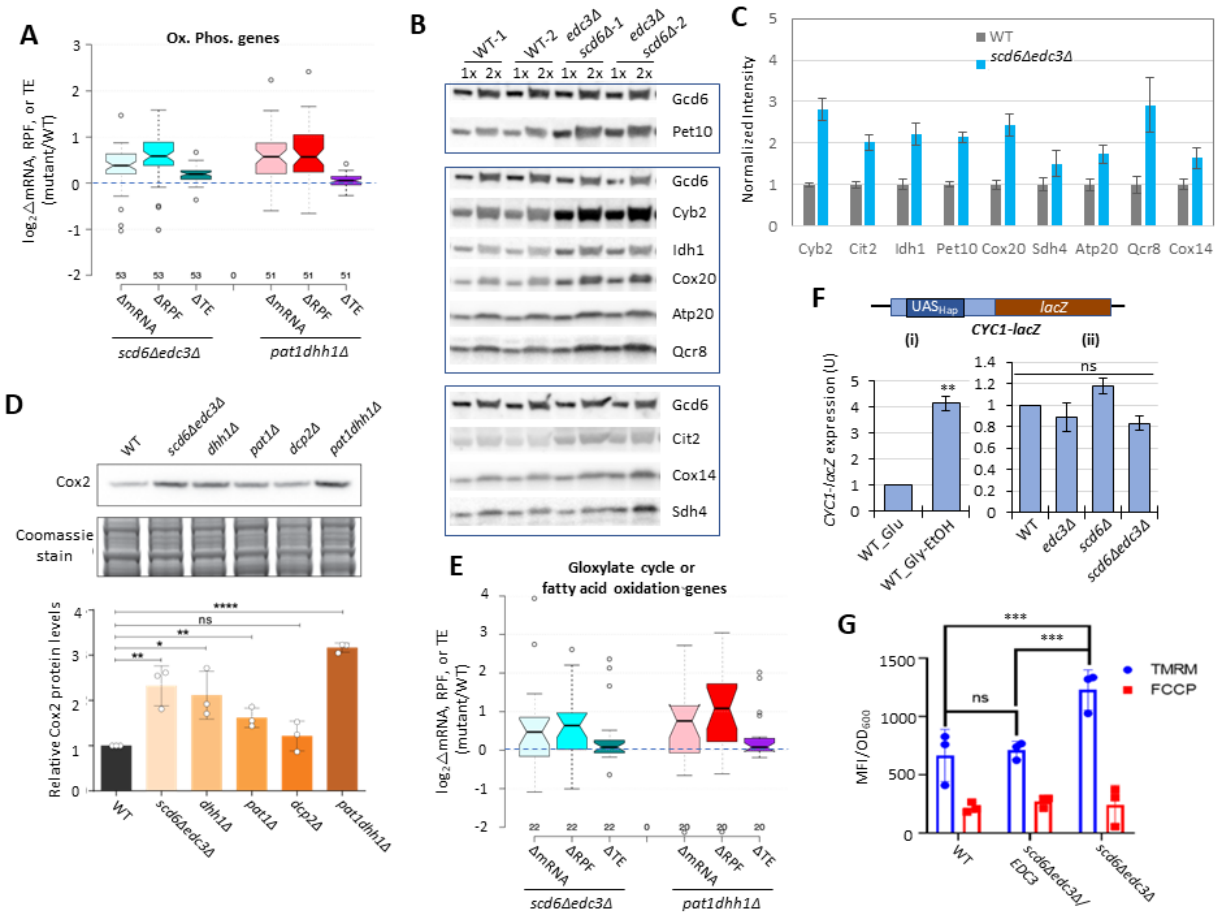

Fig. 6. Scd6/Edc3 post-transcriptionally repress proteins involved in respiration and suppress mitochondrial membrane potential in rich medium. (A) Log_2 changes in mRNA, RPFs, or TE conferred by the indicated double mutations vs. WT for 53 nuclear genes encoding mitochondrial proteins involved directly in oxidative phosphorylation. **(B-C)** Western blot analysis of 9 mitochondrial proteins and Gcd6 (examined as loading control) in WT and *scd6Δedc3Δ* strains, cultured in duplicate in YPD medium to OD_{600} of ~0.6-0.8. WCEs were extracted under denaturing conditions and aliquots corresponding to 1X or 2X amounts of WCE were loaded in successive lanes for the two replicate cultures. Immune complexes were visualized with enhanced chemiluminescence (B). Signals for each protein were quantified, normalized to the corresponding signals for Gcd6 in the same extract and expressed relative to the resulting values

for WT cells. Mean values and standard errors are plotted (C). **(D)** Western blot analysis of Cox2 in strains of the indicated genotypes in cells cultured as in (B). Cox2 signal intensity was normalized to total Coomassie-stained protein and the resulting relative Cox2 protein levels from three biological replicates were averaged and plotted. **(E)** Log_2 changes in mRNA, RPFs, or TE conferred by the indicated double mutations vs. WT for 22 genes encoding enzymes of the glyoxylate cycle or fatty acid metabolism. **(F)** Expression of the *CYC1-lacZ* reporter on plasmid pLG265, lacking UAS1 and containing the optimized version of UAS2, UAS2UP1, in the WT strain grown on SC-Ura medium containing either 2% glucose or 3% glycerol/2% ethanol as carbon sources (i), or in WT and the indicated mutant strains on SC-Ura with 2% glucose (ii). β-galactosidase activity (nmoles of o-nitrophenyl-β-D-galactopyranoside (ONPG) cleaved per min per mg of total protein) was measured in whole cell extracts for 3 biological replicates of each strain and the mean values were normalized to the mean activity measured in WT grown with glucose as carbon source. **, P-value <0.01 from student's t-test; ns, not significant. **(G)** Measurements of mitochondrial membrane potential. WT cells or transformants of the *scd6Δedc3Δ* mutant containing the *EDC3* plasmid pLfz614-7 or empty vector were cultured in SC-Ura to mid-log phase. TMRM (500 nM) was added and incubated for 30 min before samples were collected and washed once with deionized water. $\Delta\Psi_m$ was determined by measuring TMRM fluorescence intensity using flow cytometry. Data are presented in arbitrary fluorescence intensity units per OD_{600}. 2-way ANOVA was used for statistical analysis and data are given as mean values ± SD (n=3) (****p<0.0001).

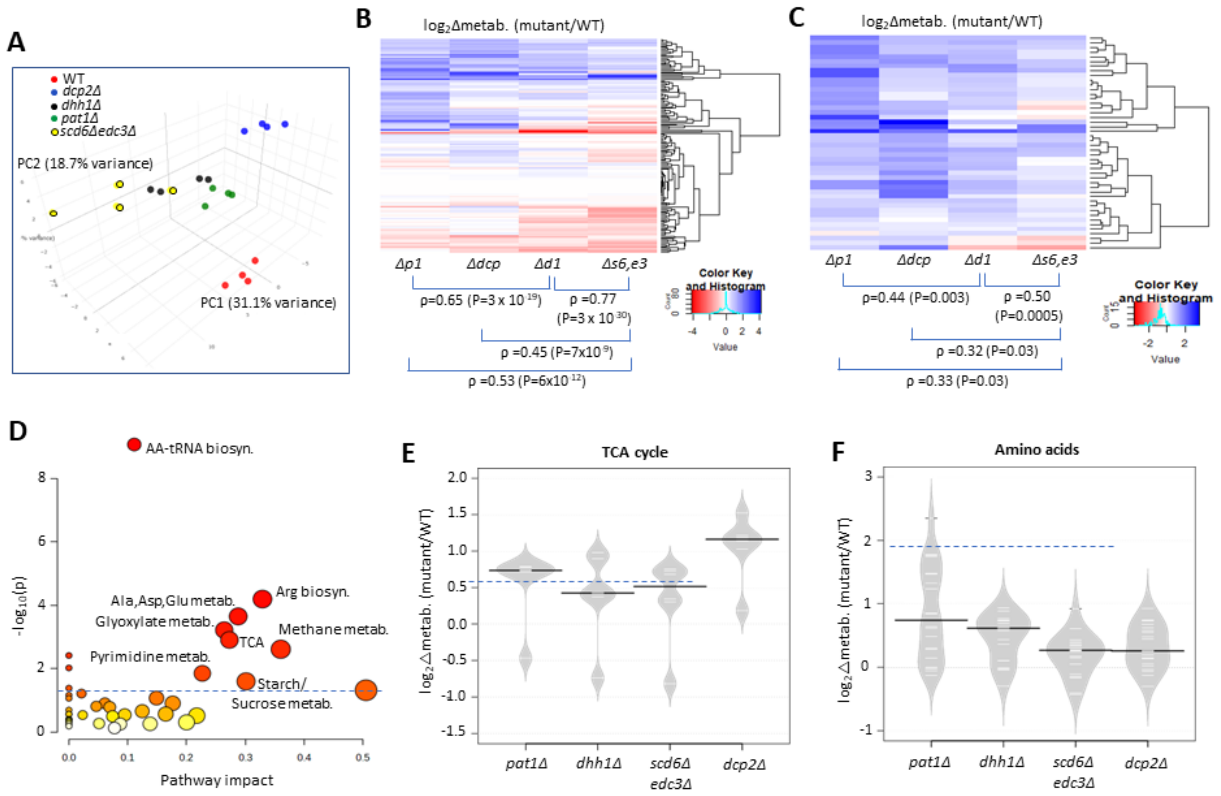

Fig. 7. Eliminating decapping activators or decapping enzyme confers similar changes in polar metabolites. (A) Principal component analysis of the levels of 147 metabolites in biological replicates of each strain. **(B-C)** Hierarchical clustering analysis of $\log_2$ changes in all 147 metabolites analyzed (B) or the 46 metabolites up-regulated in any two of the four mutants (C) conferred by the indicated mutations vs. WT, including the Spearman coefficients (ρ) and P values for the indicated correlations. **(D)** Results of pathway analysis of the 46 up-regulated metabolites described in (C) conducted at https://www.metaboanalyst.ca/MetaboAnalyst/Secure/pathway. Red ovals depict groups of metabolites significantly enriched among the set of 46 compounds, with P-value <0.05. **(E-F)** Log_2 changes in levels of TCA cycle intermediates (E) or amino acids (F) conferred by the indicated mutations vs. WT.

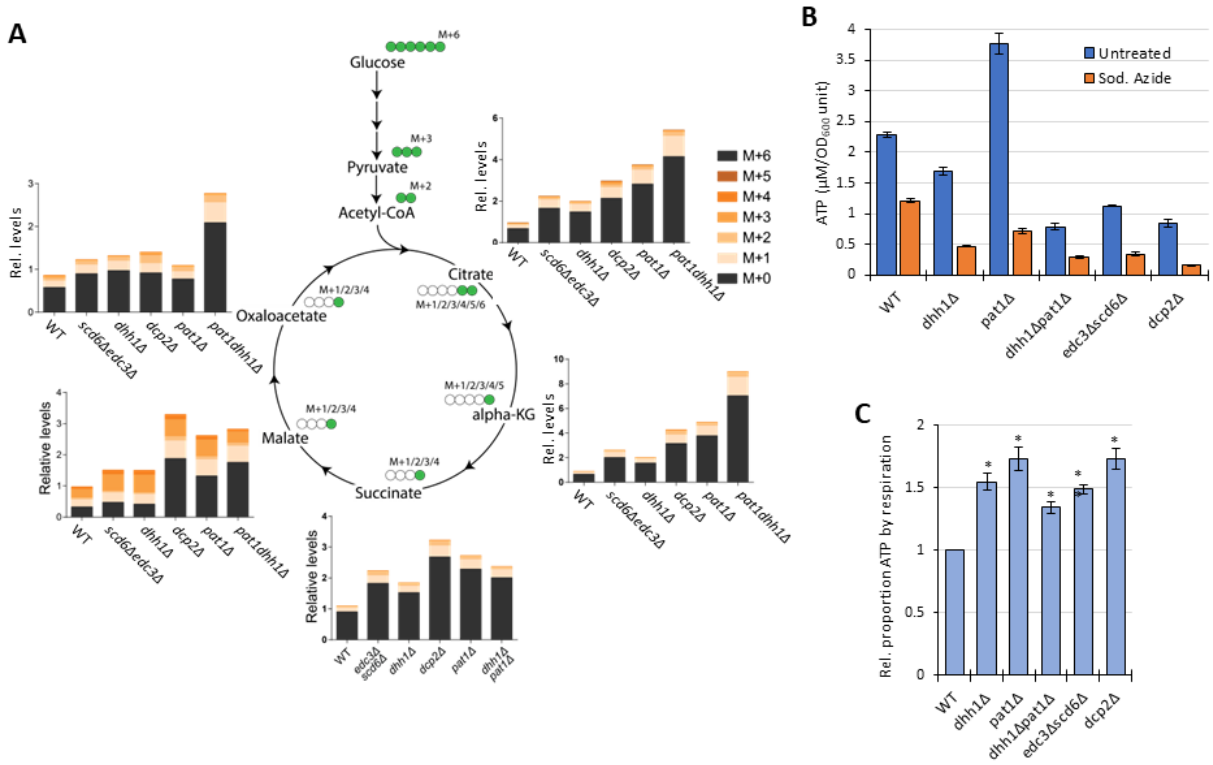

Fig. 8. Elimination of decapping activators or decapping enzyme up-regulates respiration, increasing flux from glucose into TCA cycle intermediates and proportion of ATP produced by Ox. Phos. (A) Three biological replicates of cells of each indicated genotype were cultured in YP with 2% unlabeled glucose, shifted to YP with 1% unlabeled glucose for 20 min, and pulsed with $^{13}C_6$ labelled glucose (at final concentration of 1%) for 8 min, followed by extraction of metabolites and quantification of the indicated TCA cycle intermediates by mass spectrometry. In the diagrams, green circles signify the labelled carbon atom and the notation M+1, M+2, etc. indicate the mass increase in the molecules due to the labelled carbon. The depicted labelling pattern of metabolites reflects on cycle of the TCA cycle, resulting in mass additions of M+1 and

M+2; however, across multiple cycles, a broader range of metabolite species with different mass additions will emerge. The metabolite signal intensities in all samples are expressed relative to that determined for the first replicate of the WT strain. **(B-C)** Measurements of ATP levels and proportions of total ATP impaired by azide inhibition of ETC activity. Cells cultured in YPD were treated or untreated with sodium azide for 30 min prior to harvesting. ATP levels were determined in extracts and normalized to OD_{600} units of cells for three biological replicates each of treated and untreated cell aliquots. Mean values for each strain are plotted in (B) and relative fractions of ATP in untreated samples retained following azide treatment (ATP_untreated)-(ATP_Azide)/ATP_untreated), normalized to the values determined for WT are plotted in (C) with results from a student's t-test indicated with asterisks: **, $P<0.005$; *, $P<0.05$.

SUPPLEMENTARY MATERIAL FOR:

Decapping activators Edc3 and Scd6 act redundantly with Dhh1 in nutrient-replete cells to post-transcriptionally repress starvation-induced pathways

Rakesh Kumar[1#], Fan Zhang[1#], Shreyas Niphadkar[3], Chisom Onu[2], Anil Kumar Vijjamarri[1], Miriam L. Greenberg[2], Sunil Laxman[3], and Alan G. Hinnebusch[1]

SUPPLEMENTARY TABLES

Table S1. Yeast strains employed.

Strain	Genotype	Source
255	*MATa his3Δ1 leu2Δ0 met15Δ0 ura3Δ0 edc3Δ::kanMX4*	Research Genetics
HFY114 (W303)	*MATa ade2-1 ura3-1 his3-11,15 trp1-1 leu2-3, 112 can1-100*	(1)
SYY2352	*MATa ade2-1 ura3-1 his3-11,15 trp1-1 leu2-3, 112 can1-100 scd6Δ::kanMX6*	(2)
FZY855	*MATa ade2-1 ura3-1 his3-11,15 trp1-1 leu2-3, 112 can1-100 scd6Δ::hphMX4*	This study
FZY858	*MATa ade2-1 ura3-1 his3-11,15 trp1-1 leu2-3, 112 can1-100 scd6Δ::hphMX4 edc3Δ::kanMX4*	This study
FZY862	*MATa ade2-1 ura3-1 his3-11,15 trp1-1 leu2-3, 112 can1-100 edc3Δ::kanMX4*	This study
H5217/QZY126	*MATa ade2-1 ura3-1 his3-11,15 trp1-1 leu2-3,112 can1-100 dhh1Δ::kanMX*)	(3)
F2181/ BSY3037	*MATa ade2-1 ura3-1 his3-11,15 trp1-1 leu2-3,112 can1-100 pat1Δ::HIS3*)	(4)
F2182/ YFW168	*MATa ade2-1 ura3-1 his3-11,15 trp1-1 leu2-3,112 can1-100 pat1Δ::HIS3 dhh1Δ::kanMX*	(4)
CFY1016	*MATa ade2-1 ura3-1 his3-11,15 trp1-1 leu2-3,112 can1-100 dcp2::HIS3*	(1)

Table S2. Plasmids employed.

Plasmid	Description	Source
YCplac33	s.c. *URA3* vector	(5)
YCplac111	s.c. *LEU2* vector	(5)
pLfz614-7	*EDC3* in YCplac33	This study
pLfz615-5	*SCD6* in YCplac33	This study
pLfz635-5	*EDC3* in YCplac111	This study (in case used)
pLfz636-1	*SCD6* in YCplac111	This study (in case used)
pLGADH2	*ADH2* 5' non-coding region fused to *lacZ*	(6)
pLG265	*CYC1-lacZ* reporter lacking UAS1 and containing the optimized version of UAS2, UAS2UP1	(7)
pRK4	UAS_{GATA}-*CYC1-lacZ* reporter containing the UAS from *MEP2* modified to contain additional GATA sequences	(8)

SUPPLEMENTARY FIGURES

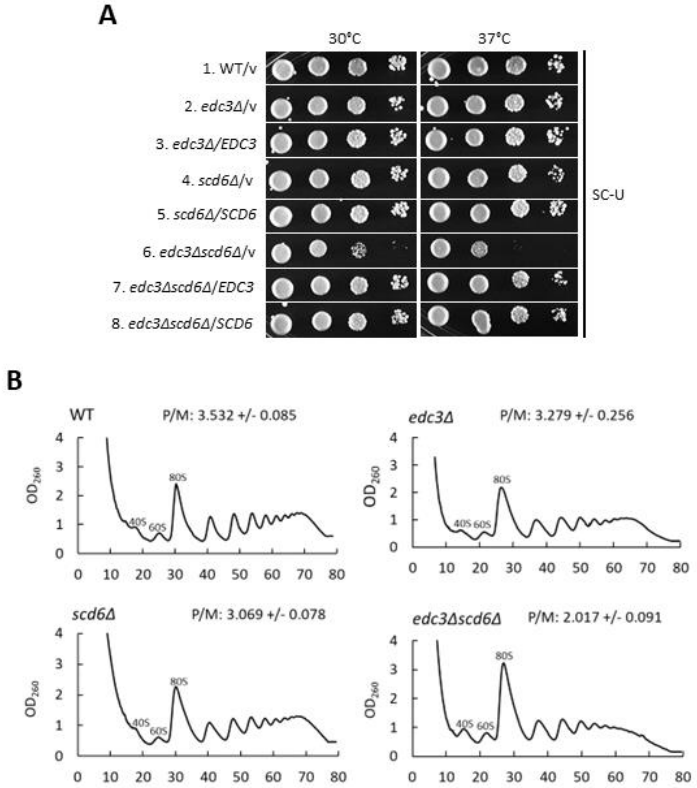

Figure S1. Combining *scd6Δ* and *edc3Δ* mutations confer synthetic reductions in cell growth and polysome assembly. (A) Serial dilutions of WT strain HFY114, *edc3Δ* strain FZY862, *scd6Δ* strain SYY2352, and *scd6Δedc3Δ* strain FZY858 transformed with empty *URA3 CEN* vector YCplac33 or derivatives of this vector containing *EDC3* (pLfz614-7) or *SCD6* (pLfz615-5) were spotted on synthetic complete plates minus uracil (SC-Ura) and incubated at the indicated temperatures.

(B) Polysome profiles of the strains in (A) but lacking plasmids cultured in YPD medium at 30°C to log-phase growth and treated with cycloheximide prior to harvesting to block run-off of elongating ribosomes during cell lysis. Cell extracts were resolved by sedimentation through 10-50% sucrose gradients, and gradients were scanned at 260 nm to yield the indicated tracings.

Average polysome/monosome ratios (P/M) from 2 biological replicates are shown, with means +/- SEMs.

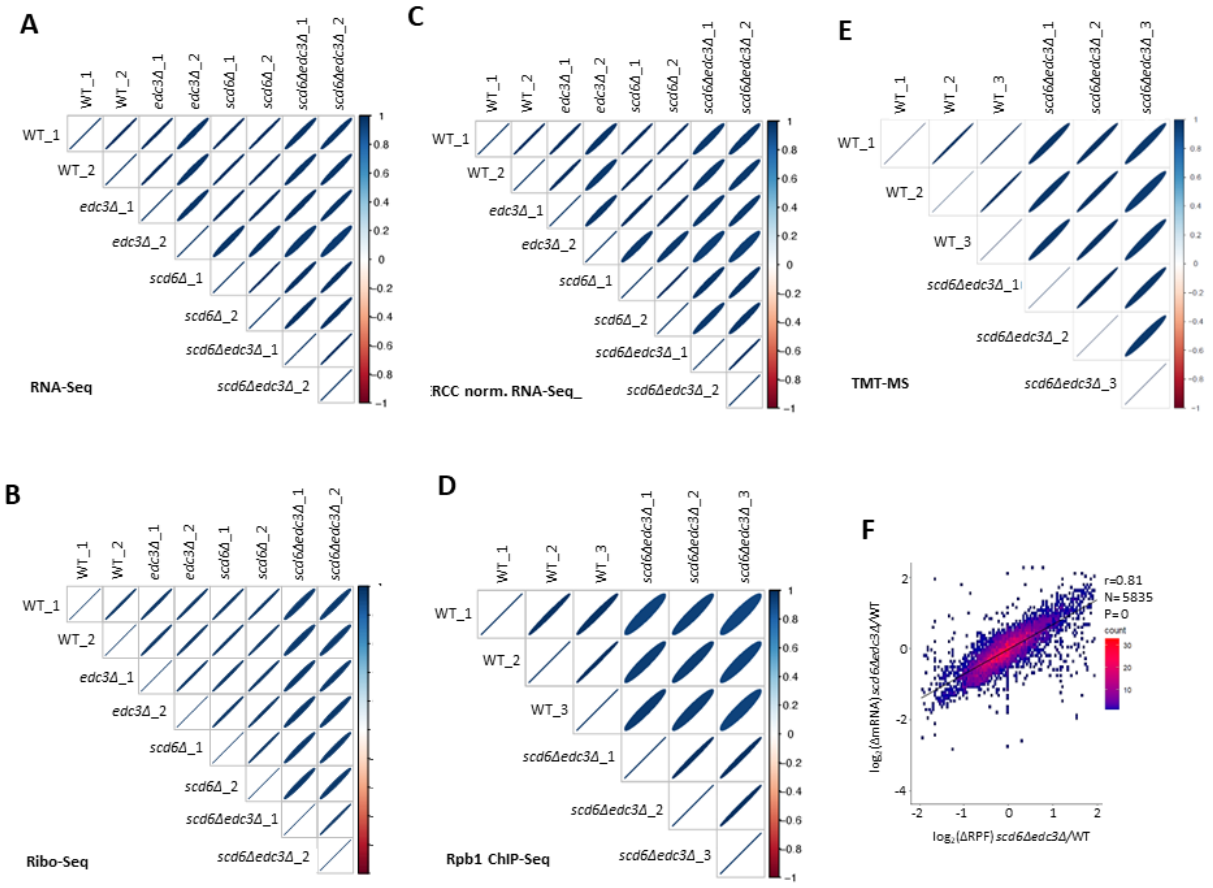

Figure S2. Reproducibility among biological replicates of RNA-Seq, Ribo-Seq, ERCC-normalized RNA-Seq, Rpb1 ChIP-seq, and TMT-MS data. (A) Correlation matrix showing Spearman correlation coefficients calculated for pair-wise comparisons of numbers of RPKM-normalized RNA-Seq reads for all expressed genes among all 8 RNA-Seq libraries generated for 2 biological replicates (_1,_2) of the indicated genotypes. The correlation coefficients between replicates are ≥0.98 and for all comparisons >0.95 with P-values of ≈0. For this and all similar plots below, the eccentricity of the ellipses are scaled parametrically to the correlation value between the two samples. **(B)** Same as (A) but for Ribo-Seq data, with correlation coefficients between replicates >0.995 and for all comparisons >0.96 with P-values of ≈0. **(C)** Same as (A) but for ERCC-normalized RNA-Seq data, with correlation coefficients between replicates >0.97 and for all comparisons >0.94 with P-values of ≈0. **(D)** Same as (A) but for Rpb1 ChIP-Seq data

comparing 3 normalized occupancies averaged across the CDS of all 5770 expressed genes, with correlation coefficients between replicates >0.98 and for all comparisons >0.91 with P-values of ≈0. **(E)** Same as (A) but for TMT-MS data, comparing $\log_2$ cyclic Loess-normalized exclusive MS1 intensities for all expressed proteins with correlation coefficients between replicates >0.96 and for all comparisons >0.95 with P-values of ≈0. **(F)** Correlation between changes in abundance of RNA vs. RPFs for 5835 expressed transcripts in the *scd6Δedc3Δ* double mutant compared to WT, calculated from RPKM-normalized RNA-Seq and Ribo-Seq reads obtained after combining data from biological replicates, with the Pearson correlation coefficient (r) and P-value of the correlation indicated.

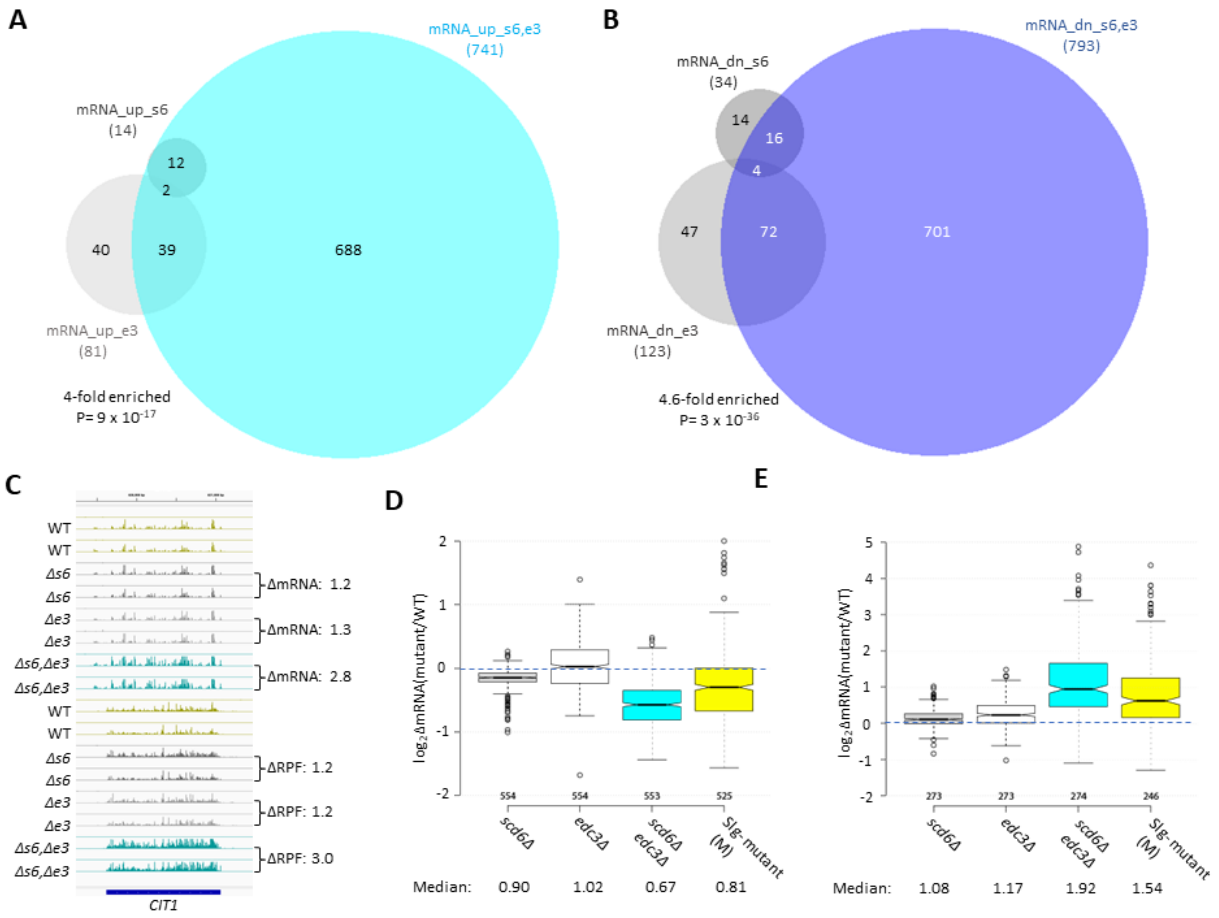

Figure S3. Functional redundancy between Scd6 and Edc3 in controlling mRNA abundance and mobilizing the ESR. (A-B) Venn diagrams of overlaps between all mRNA_up (A) and all mRNA_dn (B) groups identified in *scd6Δ, edc3Δ*, or *scd6Δedc3Δ* mutants vs. WT, with fold-enrichments and P values from the hypergeometric distribution indicated for overlapping sets. **(C)** Gene browser image showing the mRNA (top 16 tracks) and RPF (bottom 16 tracks) reads measured by ribosome profiling for two biological replicates of WT and the indicated mutants for *CIT1*, with fold-changes in mRNA or RPFs between mutant and WT indicated to the right of each track. **(D-E)** Notched box-plot analyses of $\log_2$ changes in mRNA abundance in mutant vs. WT for 585 rESR (C) and 283 iESR (D) mRNAs conferred by *scd6Δ, edc3Δ*, or *scd6Δedc3Δ* mutations and those observed for the slowest-growing yeast deletion mutants (M) analyzed previously (9). Each box

depicts the interquartile range containing 50% of the data, intersected by the median; the notch indicates a 95% confidence interval (CI) around the median. Median changes (un-logged) are shown at the bottom.

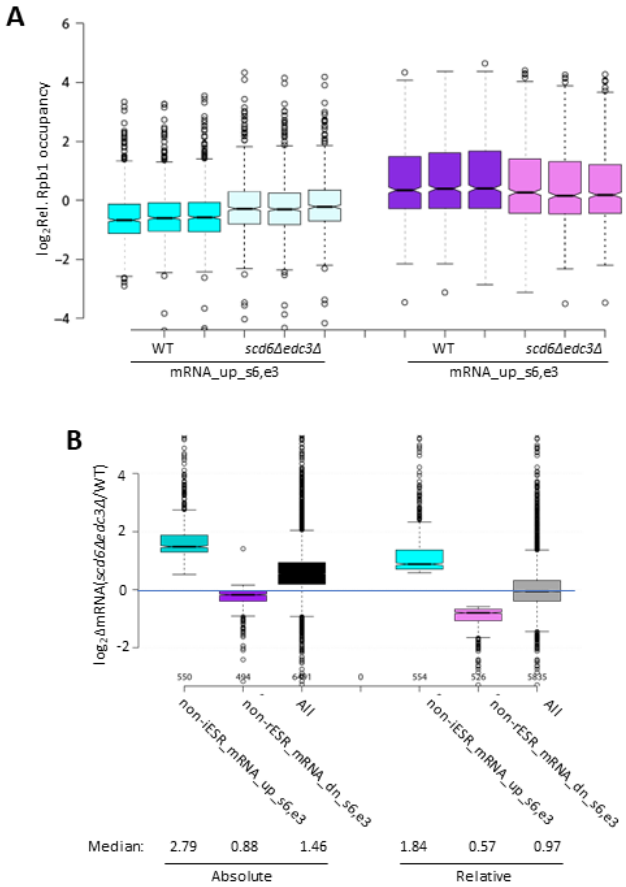

Figure S4. Reproducibility among biological replicates of Rpb1 ChIP-seq data. Log_2 values of relative Rpb1 occupancies averaged over the CDSs for three replicates of WT or *scd6Δedc3Δ* cells for the mRNAs up- or down-regulated by *scd6Δedc3Δ* vs. WT, including ESR transcripts. **(B)** Notched box-plots showing log_2 changes in absolute mRNA abundance from ERCC spike-in normalized RNA-Seq (left) or relative mRNA abundance determined by DESeq2 analysis of RNA-Seq results (right) in *scd6Δedc3Δ* vs. WT cells for all mRNAs or the 554 or 526 non-ESR mRNAs up- or down-regulated, respectively, by *scd6Δedc3Δ* vs. WT.

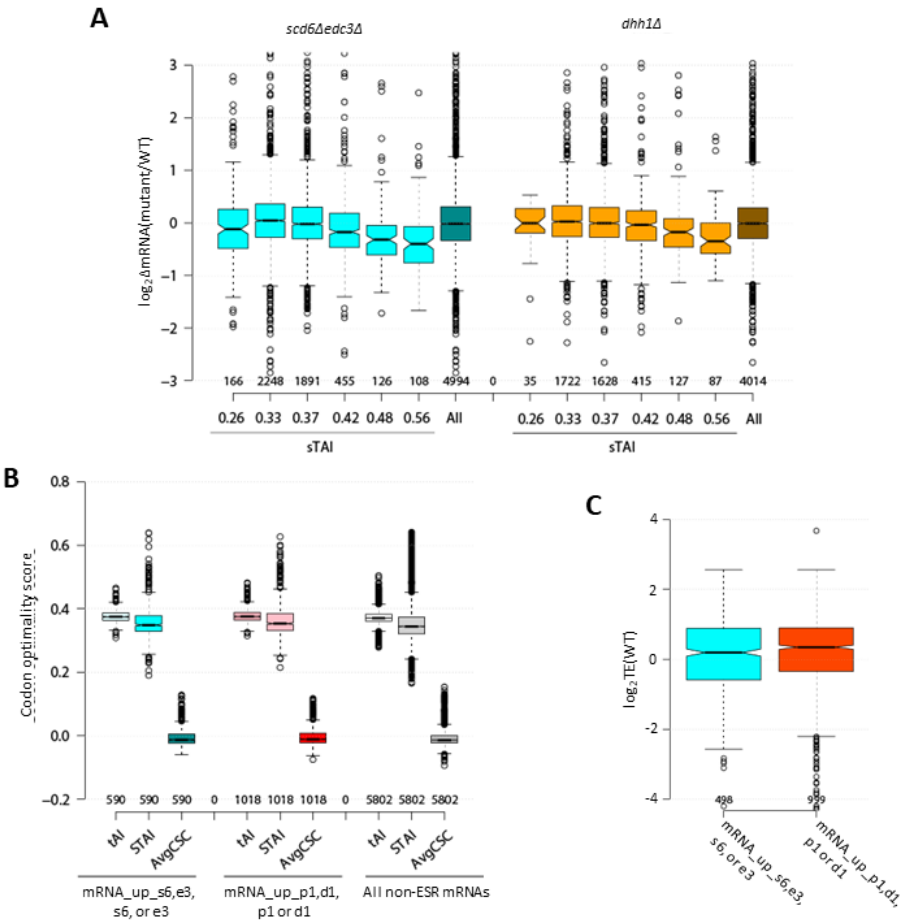

Figure S5. Average median codon optimality scores and average median TE values in WT cells for mRNAs repressed in abundance by Scd6/Edc3 or Dhh1/Pat1. (A) Notched box-plots of $\log_2\Delta$mRNA between *scd6Δedc3Δ* (left, cyan) or *dhh1Δ* (right, orange) vs. WT for 6 bins of all non-ESR mRNAs sorted according to stAI values, designated by the median stAI value for each bin, or for all non-ESR mRNAs (All). **(B)** tAI, stAI, and average CSC values for the 591 non-iESR mRNAs derepressed in abundance by the *scd6Δ, edc3Δ*, or *scd6Δedc3Δ* mutations, the 1018 non-ESR mRNAs up-regulated by the *dhh1Δ, pat1Δ*, or *pat1Δdhh1Δ* mutations, or all 5802 non-ESR mRNAs. **(C)** Log_2 values of TE determined in WT cells for the same groups of non-iESR mRNAs derepressed by the *scd6Δ, edc3Δ*, or *scd6Δedc3Δ* mutations or by the *dhh1Δ, pat1Δ*, or *pat1Δdhh1Δ* mutations analyzed in (A).

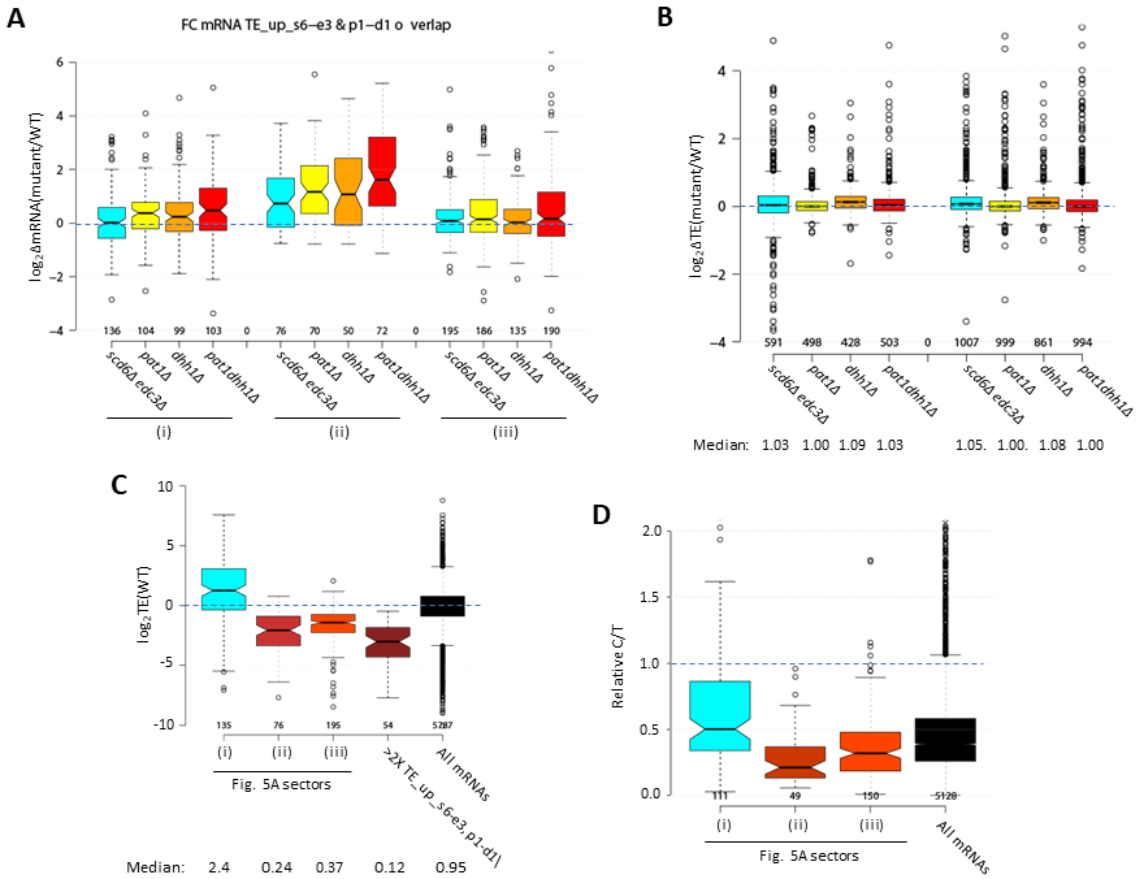

Figure S6. Properties of mRNAs translationally repressed by Scd6/Edc3 or Dhh1/Pat1. (A) Notched box-plots of $\log_2\Delta$mRNA values between the indicated mutants vs. WT for the translationally up-regulated mRNAs belonging to the specified sectors of the diagram in Fig. 5A. **(B)** Notched box-plots of $\log_2\Delta$TE values between the indicated mutants vs. WT for the mRNAs belonging to the 591 non-iESR mRNAs derepressed in abundance by *scd6Δ, edc3Δ*, or *scd6Δedc3Δ* vs. WT or the 1018 non-ESR mRNAs up-regulated by *dhh1Δ, pat1Δ*, or *pat1Δdhh1Δ* vs. WT. **(C)** Box-plot of $\log_2$ values of TE determined in WT cells for the translationally up-regulated mRNAs belonging to the specified sectors of the diagram in Fig. 5A, the 54 mRNAs showing >2-fold TE increases conferred by both *scd6Δedc3Δ* and *pat1Δdhh1Δ* mutations vs. WT, or for all mRNAs. **(D)** Box-plot of ratios of capped to total mRNA abundance in TPMs (Relative C/T) in WT cells for

for the translationally up-regulated mRNAs belonging to the specified sectors of the diagram in Fig. 5A, or for all mRNAs.

A

591 Non-iESR mRNAs w/ abundance repressed by Edc3/Scd6#			
Category	**p-value**	**k**	**f**
GO Biological process			
ATP synthesis coupled proton transport [GO:0015986]	3.23E-07	10	17
mitochondrial electron transport, cytochrome c to oxygen [GO:0006123]	1.37E-06	8	12
cristae formation [GO:0042407]	5.56E-06	5	5
ATP biosynthetic process [GO:0006754]	6.56E-06	12	31
cellular cell wall organization [GO:0007047]	7.22E-06	22	89
GO Cellular Component			
mitochondrial inner membrane [GO:0005743]	5.86E-09	45	204
mitochondrion [GO:0005739]	2.60E-08	145	1072
mitochondrial respiratory chain complex IV [GO:0005751]	5.81E-08	9	12
fungal-type cell wall [GO:0009277]	3.19E-06	22	85
MIPS Functional Classification			
electron transport and membrane-associated energy conservation [02.11]	<1e-14	34	58
electron transport [20.01.15]	2.02E-10	28	83
aerobic respiration [02.13.03]	4.75E-09	25	77
energy generation (e.g. ATP synthase) [02.45.15]	3.16E-08	12	21
respiration [02.13]	8.95E-06	17	59
(ii) ***212 mRNAs translationaly repressed by Edc3/Scd6#***			
GO Biological process			
asparagine catabolic process [GO:0006530]	5.04E-06	4	5
cellular aldehyde metabolic process [GO:0006081]	1.28E-05	5	11
GO Cellular Component			
cell wall [GO:0005618]	8.85E-06	11	68
extracellular region [GO:0005576]	9.09E-06	13	95
ribosome [GO:0005840]	1.70E-05	25	310
MIPS Functional Classification			
degradation of asparagine [01.01.06.02.02]	5.04E-06	4	5
fermentation [02.16]	6.92E-06	7	24

B

1018 Non-iESR mRNAs w/ abundance repressed by Pat1/Dhh1#			
Category	**p-value**	**k**	**f**
GO Biological process			
tricarboxylic acid cycle [GO:0006099]	2.87E-08	18	30
mitochondrial respiratory chain complex IV assembly [GO:0033617]	4.03E-06	10	14
GO Cellular Component			
fungal-type cell wall [GO:0009277]	3.12E-08	34	85
cell wall [GO:0005618]	9.82E-07	27	68
extracellular region [GO:0005576]	2.29E-06	33	95
mitochondrion [GO:0005739]	4.81E-06	215	1072
mitochondrial inner membrane [GO:0005743]	1.20E-05	55	204
plasma membrane [GO:0005886]	1.93E-05	83	350
MIPS Functional Classification			
tricarboxylic-acid pathway (citrate cycle, Krebs cycle, TCA cycle) [02.10]	5.86E-08	18	31
electron transport and membrane-associated energy conservation [02.11]	3.90E-07	25	58
aerobic respiration [02.13.03]	1.43E-06	29	77
(ii) ***274 mRNAs translationaly repressed by Pat1/Dhh1#***			
GO Molecular Function			
sequence-specific DNA binding [GO:0043565]	3.85E-06	21	165
GO Biological process			
cellular aldehyde metabolic process [GO:0006081]	1.88E-06	6	11
allantoin catabolic process [GO:0000256]	2.33E-06	5	7
transmembrane transport [GO:0055085]	6.78E-06	30	303
flocculation [GO:0000128]	1.40E-05	4	5
GO Cellular Component			
cell wall [GO:0005618]	3.29E-06	13	68
extracellular region [GO:0005576]	7.03E-06	15	95
plasma membrane [GO:0005886]	4.41E-05	31	350
MIPS Functional Classification			
C-compound and carbohydrate metabolism [01.05]	4.18E-07	27	223
fermentation [02.16]	3.27E-06	8	24
catabolism of nitrogenous compounds [01.02.02.09]	1.40E-05	4	5
metabolism of nonprotein amino acids [01.20.17.01]	2.52E-05	5	10
osmosensing and response [34.11.03.13]	7.03E-05	8	35
proton driven symporter [20.03.02.02.01]	7.07E-05	3	3

C

853 mRNAs with ribosome occupancy repressed by Edc3/Scd6#			
GO Biological process			
response to stress [GO:0006950]	2.57E-11	51	152
thiamine biosynthetic process [GO:0009228]	9.28E-07	11	17
mitochondrial respiratory chain complex IV assembly [GO:0033617]	1.05E-05	9	14
glycogen biosynthetic process [GO:0005978]	2.30E-05	8	12
mitochondrial electron transport, cytochrome c to oxygen [GO:0006123]	2.30E-05	8	12
GO Cellular Component			
mitochondrion [GO:0005739]	2.81E-13	227	1072
mitochondrial inner membrane [GO:0005743]	1.39E-08	56	204
extracellular region [GO:0005576]	1.45E-05	28	95
mitochondrial intermembrane space [GO:0005758]	1.60E-05	16	40
plasma membrane enriched fraction [GO:0001950]	1.78E-05	26	86
mitochondrial respiratory chain complex IV [GO:0005751]	2.30E-05	8	12
cell wall [GO:0005618]	2.43E-05	22	68
fungal-type cell wall [GO:0009277]	4.31E-05	25	85
MIPS Functional Classification			
electron transport and membrane-associated energy conservation [02.11]	1.24E-13	31	58
metabolism of energy reserves (e.g. glycogen, trehalose) [02.19]	1.81E-11	28	56
sugar, glucoside, polyol and carboxylate catabolism [01.05.02.07]	5.92E-11	34	81
stress response [32.01]	1.15E-09	50	162
aerobic respiration [02.13.03]	2.98E-08	29	77
electron transport [20.01.15]	2.01E-07	29	83
C-compound and carbohydrate metabolism [01.05]	3.82E-07	56	223
oxidative stress response [32.01.01]	4.14E-07	22	55
sugar, glucoside, polyol and carboxylate anabolism [01.05.02.04]	1.94E-06	16	35
oxidation of fatty acids [02.25]	1.67E-05	7	9
glutathione conjugation reaction [32.07.07.03]	3.56E-05	5	5
detoxification by modification [32.07.03]	0.0001015	6	8

D

1350 mRNAs with ribosome occupancy repressed by Pat1/Dhh1#			
GO Biological process			
tricarboxylic acid cycle [GO:0006099]	6.14E-09	21	30
response to stress [GO:0006950]	4.06E-06	55	152
glycogen biosynthetic process [GO:0005978]	5.45E-06	10	12
cellular response to oxidative stress [GO:0034599]	1.77E-05	29	67
GO Cellular Component			
mitochondrion [GO:0005739]	3.75E-12	305	1072
fungal-type cell wall [GO:0009277]	5.62E-12	46	85
extracellular region [GO:0005576]	1.06E-08	44	95
cell wall [GO:0005618]	1.15E-08	35	68
plasma membrane [GO:0005886]	7.34E-05	101	350
MIPS Functional Classification			
metabolism of energy reserves (e.g. glycogen, trehalose) [02.19]	8.14E-09	31	56
C-compound and carbohydrate metabolism [01.05]	1.75E-08	81	223
oxidative stress response [32.01.01]	1.05E-07	29	55
tricarboxylic-acid pathway (citrate cycle, Krebs cycle, TCA cycle) [02.10]	7.92E-07	19	31
stress response [32.01]	1.42E-06	59	162
electron transport and membrane-associated energy conservation [02.11]	1.82E-06	28	58
aerobic respiration [02.13.03]	6.14E-06	33	77
metabolism of vitamins, cofactors, and prosthetic groups [01.07]	7.04E-06	22	43
sugar, glucoside, polyol and carboxylate catabolism [01.05.02.07]	7.75E-06	34	81
osmotic and salt stress response [32.01.03]	3.27E-05	26	

Figure S7. mRNAs repressed in abundance or translation by Scd6/Edc3 or Dhh1/Pat1 are enriched for common functional categories, including Ox. Phos. proteins and cell wall

components. (A-B) Functional categories showing enrichment for genes encoding the 591 non-iESR mRNAs derepressed in abundance by *scd6Δ, edc3Δ*, or *scd6Δedc3Δ* vs. WT or the 1018 non-ESR mRNAs up-regulated by *dhh1Δ, pat1Δ*, or *pat1Δdhh1Δ* vs. WT, using color-coding to indicate related functions or cellular components. **(C-D)** Functional categories showing enrichment for genes encoding the 853 mRNAs with RPFs up-regulated by *scd6Δ, edc3Δ*, or *scd6Δedc3Δ* vs. WT or the 1350 mRNAs with RPFs up-regulated by *dhh1Δ, pat1Δ*, or *pat1Δdhh1Δ* vs. WT, conducted using the Web-based tool FunSpec and applying the Bonferroni correction and $P<0.05$ cutoff.

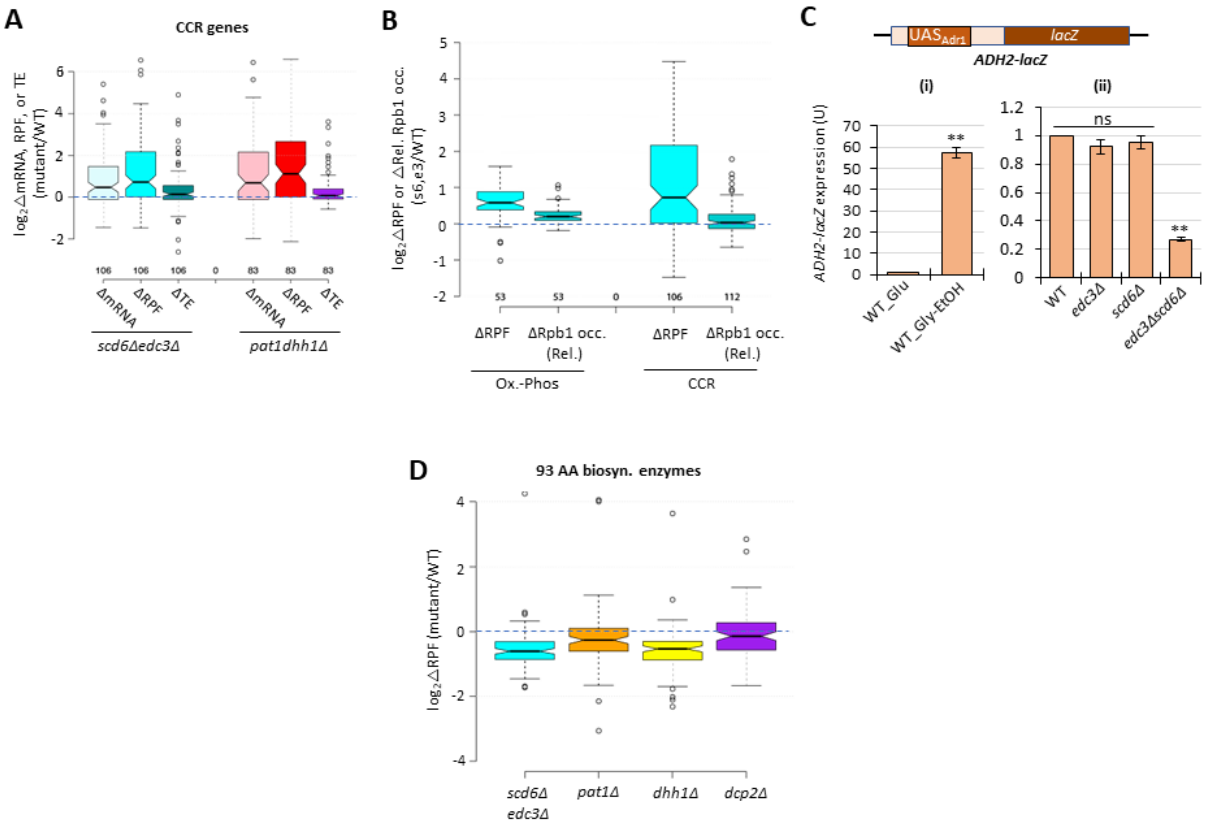

Figure S8. Scd6/Edc3 post-transcriptionally repress carbon-catabolite-repressed (CCR) genes in rich medium. (A) Log_2 changes in mRNA, RPFs, or TE conferred by the indicated double mutations vs. WT for 106 genes subject to carbon catabolite repression or activated by transcription factors Adr1 or Cat8. **(B)** Notched box-plots showing log_2ΔRPFs or log_2ΔRpb1 relative occupancies averaged over the CDSs in *scd6Δedc3Δ* vs. WT cells for the same Ox-Phos. (left) or CCR genes (right) analyzed in Figures 6A and S7A, respectively. **(C)** Expression of the *ADH2-lacZ* reporter on plasmid pLGADH2, containing the entire *ADH2* 5' non-coding region, in the WT strain grown on SC-Ura medium containing either 2% glucose or 3% glycerol/2% ethanol as carbon sources (i), or in WT and the indicated mutant strains on SC-Ura cultured with 2% glucose (ii). For (ii), mean values of β-galactosidase activity measured for 3 biological replicates of each strain were

normalized to the mean value measured for WT cells. **, P-value <0.01 from student's t-test; ns, not significant. **(D)** Log_2 changes in RPFs for 93 genes encoding amino acid biosynthetic enzymes in the indicated mutants vs. WT.

Gene id	Gene	$\log_2\Delta$mRNA (*scd6Δ*/WT)	FDR	$\log_2\Delta$mRNA (*edc3Δ*/WT)	FDR	$\log_2\Delta$mRNA (*scd6Δedc3Δ*/WT)	FDR	Targeted by
YGL222C	*EDC1*	0.415787885	4.48E-05	0.316768752	0.257140053	1.98410287	1.86E-155	Dhh1
YGL056C	*SDS23*	0.05093765	0.764889364	-0.201352497	0.530102611	0.472035691	8.08E-10	Dhh1
YDR343C	*HXT6*	0.328862276	0.422677908	0.683203554	0.035918099	2.593164006	4.20E-28	Dhh1/Pat1
YFL014W	*HSP12*	0.731412062	0.033263692	0.885066918	0.115640255	6.847403632	0	Dhh1/Pat1

Figure S9. Synthetic genetic derepression of four Dhh1 target mRNAs on combining *scd6Δ* and *edc3Δ* mutations. RNA-seq results obtained here for the four Dhh1 target mRNAs, two of which were designated as Pat1 targets as well, identified by He et al. (2022), in the *scd6Δ, edc3Δ,* and *scd6Δedc3Δ* mutants versus WT. The $\log_2\Delta$mRNA values for each of the three mutants vs. WT are listed together with the FDR values and color-coded according to derepression ratios.

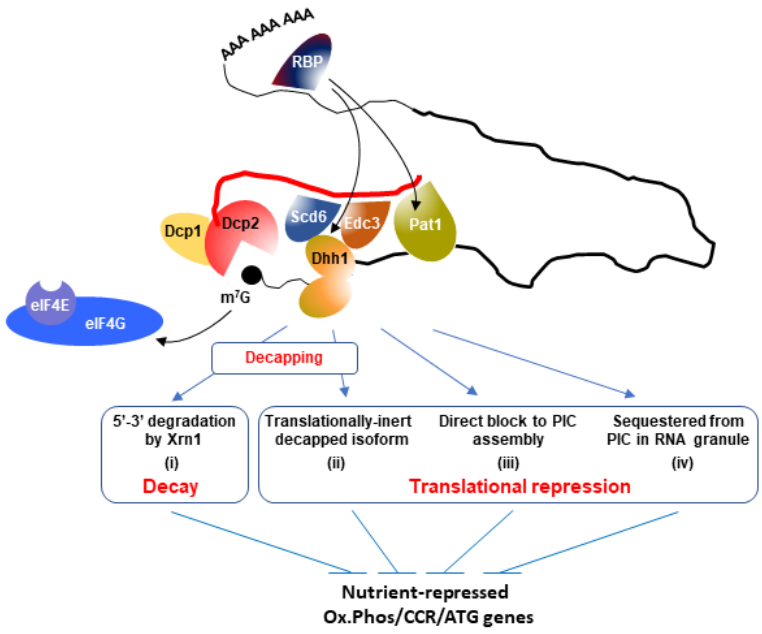

Figure S10. Hypothetical model to explain concerted repression of mRNA abundance or translation of particular mRNAs by decapping activators Scd6, Edc3, Dhh1, and Pat1. A complex of Dcp1:Dcp2 containing Scd6/Edc3, Pat1/Dhh1, or different combinations of these factors, is recruited to target mRNAs, possibly by a sequence-specific RNA-binding protein (RBP) binding to the 3'UTR. In agreement with a recent proposal (10), the recruitment of Dhh1 is enhanced by its redundant interactions with Scd6 or Edc3, which interact with the same segment of the Dcp2 CTT, whereas Pat1 is recruited independently to a distinct region of the CTT. One outcome of association of the decapping complex with an mRNA is activation of decapping with attendant 5'-3' degradation by Xrn1 occurring without detectable repression of translation (i). A different outcome is translational repression by decapping wherein degradation by Xrn1 is inefficient and decapped intermediates accumulate that cannot bind the cap-binding initiation factors eIF4E and eIF4G (depicted as subunits of eIF4F excluded from the

m^7G mRNA cap) and thus persist as translationally inert isoforms (ii). Alternatively, decapping may not occur and the decapping complex competes with the cap-binding initiation factors to selectively inhibit translation initiation (iii), a fate that could be favored by sequestration of the transcript in RNA granules in a manner facilitated by the decapping activator proteins (iv).

SUPPLEMENTARY FILES

File S1: Parallel RNA-Seq and Ribo-Seq analysis of decapping mutants, gene groups dysregulated in decapping mutants or belonging to specific functional categories, and capped/total mRNA ratios, codon optimality scores, codon protection indices, and Dhh1 occupancy values for all mRNAs. Sheets 1-7 labeled "mutant vs WT all comp" contain the processed data from Ribo-seq and RNA-seq analysis of 2 or 3 biological replicates of each strain listing the fold-changes in mRNA, RPFs, or TE between the relevant mutant vs. WT with the P-values and adjusted P-values (FDRs) assigned by DESeq2 analysis. The data for *dhh1Δ, dcp2Δ* (3)*, pat1Δ,* and *pat1Δdhh1Δ* mutants (8) were reported previously. Sheet "Gene groups_mRNA analysis" contains the lists of mRNAs (identified by systematic gene name) that are up-regulated or down-regulated in abundance by ≥1.5-fold at FDR < 0.05 in the *scd6Δ, edc3Δ,* or *scd6Δedc3Δ* mutants vs. WT, either including or excluding iESR mRNAs for up-regulated transcripts or rESR mRNAs for down-regulated transcripts, as indicated. It also lists the transcripts belonging to the three sectors of Figs. 1B-C, the iESR and rESR transcripts defined previously (11), and all of the non-iESR mRNAs up-regulated by ≥1.5-fold at FDR < 0.05 in *dhh1Δ, pat1Δ,* or *pat1Δdhh1Δ* mutants, as well as those equally up-regulated by the *dcp2Δ* mutation. Sheet "Gene groups_TE analysis" contains the lists of mRNAs that are up-regulated or down-regulated in TE by ≥1.41-fold at FDR < 0.10 in the different mutants vs. WT. Sheet "Gene groups_RPF analysis" contains the lists of mRNAs that are up-regulated or down-regulated in RPFs by ≥1.5-fold at FDR < 0.05 in the different mutants vs. WT. Sheet "Pathway gene groups" lists the genes involved in specific pathways (eg. Ox. Phos.) analyzed for changes in expression

or translation. Sheet “Codon Opt Scores nonESR mRNAs” lists the tRNA adaptation index (tAI), species-specific tRNA adaptation index (stAI), and the average codon stabilization coefficient (AvgCSC) for all non-ESR yeast genes (12,13). Sheet “Codon Protection Indices” lists the CPI values for all genes determined previously (14). Sheet “Capped to Total RNA ratios” lists the ratios of TPMs determined by CAGE sequencing of capped mRNAs (C) to TPMs determined by parallel RNA-seq of the same total RNA samples for 5129 genes, determined previously for *dhh1Δ* and WT cells (8). Sheet “Dhh1 occ enrich scores” lists the relative Dhh1 occupancies (enrichment scores) determined globally for yeast mRNAs by RIP-seq analysis (15) for the 3686 transcripts for which both Dhh1 enrichment score and Ribo-seq and RNA-seq data from the *dhh1Δ* vs. WT comparison (3) are available. Sheet “IGV tracks” lists the results of ribosome profiling of the *scd6Δ, edc3Δ,* and *scd6Δedc3Δ* mutants vs. WT for the genes selected for gene-browser depictions.

File S2: Relative and spike-in normalized Rpb1 occupancies from ChIP-seq analysis. Sheets 1-2 labeled "Relative occs._replicates” and “Relative occs._ Reps._averaged” contain the processed data from ChIP-Seq analysis of Rpb1 in three biological replicates of WT and *scd6Δedc3Δ* strains and the averaged data from combining the replicates, respectively, listing the relative occupancies averaged over the coding sequences for each expressed gene normalized to the average occupancy on each chromosome. Sheet “*S. pombe* norm. factor calcs,” lists the calculations of normalization factors obtained from total numbers of reads aligned to the *S. pombe* genome for each chromatin sample spiked-in with equal aliquots of *S. pombe* chromatin prior to immunoprecipitation with Rpb1 antibodies. Factors are calculated for each individual

replicate (col. E) or for the combined replicates for each strain (col. G). Sheets “Normalized occs._replicates” and “Normalized occs._reps._avged” lists the spike-in normalized Rpb1 occupancies calculated for each replicate or the combined replicates for each strain, respectively, calculated using the respective normalization factors for individual or combined replicates determined in the previous two sheets.

File S3: ERCC spike-in normalized RNA-Seq data. Sheet 1 lists the numbers of reads for each ERCC molecule identified in each RNA sample and calculations of the normalization factors for each sample. Sheet 2 lists the un-normalized reads for each yeast gene in each RNA sample, the ERCC-normalized reads for each sample, and the density of normalized reads for each gene calculated by normalizing for CDS lengths. Sheets 2-4 lists processed data from DESeq2, including $\log_2\Delta$ mRNA, P-value and adj. P-value determined for each gene in the indicated mutant vs. WT strain, obtained by setting the size factor to unity.

File S4: TMT-MS data. Processed data from TMT-MS analysis of *scd6Δedc3Δ* vs. WT strains. Sheet **“All proteins data” lists the normalized MS intensities of peptides for each expressed gene in three replicates each of WT (L-N) and** *scd6Δedc3Δ* (M-Q) strains and the calculated $\log_2$ fold-changes in protein expression and statistics in the *scd6Δedc3Δ* vs. WT comparison for all expressed proteins. Sheet “log2FC_protein (s6,e3 v WT)” extracts the data from columns B, Q, W, and X from the previous sheet.

File S5: Source data for Western blot analysis. Sheet "Fig. 6B-C Western analysis" lists averages of band intensities normalized to the loading control (Gcd6) on the same blots and the corresponding S.E.M. values calculated from the replicates for each protein analyzed in Fig. 6B-C. Sheet "Fig. 6D Western analysis" lists the Cox2 band intensities normalized to total stained proteins and the ratios of normalized Cox2 for each mutant vs. WT.

File S6: Source data for *lacZ* reporter assays. Lists the specific activities of β-galactosidase determined from three biological replicates of each strain harboring the *CYC1-lacZ* or *ADH2-lacZ* reporters analyzed in Figs. 6F and S7C, respectively.

File S7: Source data for metabolomics of polar compounds of intermediary metabolism. Sheets 1-4 list the statistical analyses of changes in metabolite concentrations in four biological replicates of the indicated four mutants vs. the WT determined in parallel for all 20 samples of metabolite extracts. Sheet 5 summarizes the $\log_2$ fold-changes in metabolite levels and corresponding P-values for all 147 metabolites detected in for each of the four mutants. Sheet 6 lists the 46 metabolites up-regulated in any two of the four mutants (analyzed in Fig. 7C), TCA cycle intermediates, and amino acids. Sheet 7 lists 93 amino acid biosynthetic genes interrogated in Fig. S8D.

File S8. Source data for glucose flux analysis. In Sheet 2 "raw intensity", the numbers indicate the signal intensities (areas under the peaks from mass spectrometry) of the metabolite listed in column A in the three biological replicates of the indicated mutant or WT strains. In the

subsequent sheets, raw data from Sheet 2 is collated for the different labeled isoforms of the indicated metabolite in the upper eight rows, and the proportion of the metabolite comprised of each isoform is given in the lower rows for the different samples. The "_N" labelling indicates the label addition in the metabolite, ie. _1 indicates mass addition of 1 labelled carbon, _2 indicates mass addition of 2 labelled carbons). Please let me know if you have any doubts regarding this.

File S9. Source data for measurements of cellular ATP content. Sheets 2-3 provide source data for measurements of ATP content in three biological replicates of the indicated five mutants vs. WT and the fraction of total ATP content that is eliminated by inhibiting respiration by sodium azide treatment. Sheet 4 shows the standard curve produced using pure ATP employed to determine the ATP content in cell extracts.

SUPPLEMENTARY REFERENCES

1. He, F., Li, X., Spatrick, P., Casillo, R., Dong, S. and Jacobson, A. (2003) Genome-wide analysis of mRNAs regulated by the nonsense-mediated and 5' to 3' mRNA decay pathways in yeast. *Mol Cell*, **12**, 1439-1452.
2. He, F. and Jacobson, A. (2015) Control of mRNA decapping by positive and negative regulatory elements in the Dcp2 C-terminal domain. *RNA*, **21**, 1633-1647.
3. Zeidan, Q., He, F., Zhang, F., Zhang, H., Jacobson, A. and Hinnebusch, A.G. (2018) Conserved mRNA-granule component Scd6 targets Dhh1 to repress translation initiation and activates Dcp2-mediated mRNA decay in vivo. *PLoS Genet*, **14**, e1007806.

4. Charenton, C., Gaudon-Plesse, C., Fourati, Z., Taverniti, V., Back, R., Kolesnikova, O., Seraphin, B. and Graille, M. (2017) A unique surface on Pat1 C-terminal domain directly interacts with Dcp2 decapping enzyme and Xrn1 5'-3' mRNA exonuclease in yeast. *Proc Natl Acad Sci U S A*, **114**, E9493-E9501.

5. Gietz, R.D. and Sugino, A. (1988) New yeast-Escherichia coli shuttle vectors constructed with in vitro mutagenized yeast genes lacking six-base pair restriction sites. *Gene*, **74**, 527-534.

6. Sloan, J.S., Dombek, K.M. and Young, E.T. (1999) Post-translational regulation of Adr1 activity is mediated by its DNA binding domain. *J Biol Chem*, **274**, 37575-37582.

7. Forsburg, S.L. and Guarente, L. (1989) Identification and characterization of HAP4: a third component of the CCAAT-bound HAP2/HAP3 heteromer. *Genes Dev*, **3**, 1166-1178.

8. Vijjamarri, A.K., Gupta, N., Onu, C., Niu, X., Zhang, F., Kumar, R., Lin, Z., Greenberg, M.L. and Hinnebusch, A.G. (2023) mRNA decapping activators Pat1 and Dhh1 regulate transcript abundance and translation to tune cellular responses to nutrient availability. *Nucleic Acids Res*.

9. O'Duibhir, E., Lijnzaad, P., Benschop, J.J., Lenstra, T.L., van Leenen, D., Groot Koerkamp, M.J., Margaritis, T., Brok, M.O., Kemmeren, P. and Holstege, F.C. (2014) Cell cycle population effects in perturbation studies. *Mol Syst Biol*, **10**, 732.

10. He, F., Wu, C. and Jacobson, A. (2022) Dcp2 C-terminal cis-binding elements control selective targeting of the decapping enzyme by forming distinct decapping complexes. *Elife*, **11**.

11. Gasch, A.P., Spellman, P.T., Kao, C.M., Carmel-Harel, O., Eisen, M.B., Storz, G., Botstein, D. and Brown, P.O. (2000) Genomic expression programs in the response of yeast cells to environmental changes. *Mol Biol Cell*, **11**, 4241-4257.

12. Presnyak, V., Alhusaini, N., Chen, Y.H., Martin, S., Morris, N., Kline, N., Olson, S., Weinberg, D., Baker, K.E., Graveley, B.R. *et al.* (2015) Codon optimality is a major determinant of mRNA stability. *Cell*, **160**, 1111-1124.

13. Radhakrishnan, A., Chen, Y.H., Martin, S., Alhusaini, N., Green, R. and Coller, J. (2016) The DEAD-Box Protein Dhh1p Couples mRNA Decay and Translation by Monitoring Codon Optimality. *Cell*, **167**, 122-132 e129.

14. Pelechano, V., Wei, W. and Steinmetz, L.M. (2015) Widespread Co-translational RNA Decay Reveals Ribosome Dynamics. *Cell*, **161**, 1400-1412.

15. Miller, J.E., Zhang, L., Jiang, H., Li, Y., Pugh, B.F. and Reese, J.C. (2018) Genome-Wide Mapping of Decay Factor-mRNA Interactions in Yeast Identifies Nutrient-Responsive Transcripts as Targets of the Deadenylase Ccr4. *G3 (Bethesda)*, **8**, 315-330.